Chimpanzee Brain Morphometry Utilizing Standardized MRI Preprocessing and Macroanatomical Annotations

Author list

Sam Vickery[1,2], William D. Hopkins[3], Chet C. Sherwood[4], Steven J. Schapiro[3,5], Robert D. Latzman[6], Svenja Caspers[7,8,9], Christian Gaser[10,11], Simon B. Eickhoff[1,2], Robert Dahnke[10,11,12]*, Felix Hoffstaedter[1,2]* (*equal contribution)

1 Institute of Systems Neuroscience, Medical Faculty, Heinrich-Heine-University, Düsseldorf, Germany.

2 Institute of Neuroscience and Medicine (INM-7) Research Centre Jülich, Jülich, Germany

3 Keeling Center for Comparative Medicine and Research, The University of Texas MD Anderson Cancer Center, Bastrop, Texas

4 Department of Anthropology and Center for the Advanced Study of Human Paleobiology, The George Washington University, Washington, DC, USA.

5 Department of Experimental Medicine, University of Copenhagen, Copenhagen, Denmark

6 Department of Psychology, Georgia State University, Atlanta, GA, USA

7 Institute of Neuroscience and Medicine (INM-1), Research Centre Jülich, Jülich, Germany

8 Institute for Anatomy I, Medical Faculty, Heinrich-Heine-University, Düsseldorf, Germany

9 JARA-BRAIN, Jülich-Aachen Research Alliance, Jülich, Germany

10 Structural Brain Mapping Group, Department of Neurology, Jena University Hospital, Jena, Germany

11 Structural Brain Mapping Group, Department of Psychiatry and Psychotherapy, Jena University Hospital, Jena, Germany

12 Center of Functionally Integrative Neuroscience, Department of Clinical Medicine, Aarhus University, Denmark

Abstract

Chimpanzees are among the closest living relatives to humans and, as such, provide a crucial comparative model for investigating primate brain evolution. In recent years, human brain mapping has strongly benefited from enhanced computational models and image processing pipelines that could also improve data analyses in animals by using species-specific templates. In this study, we use structural MRI data from the National Chimpanzee Brain Resource (NCBR) to develop the chimpanzee brain reference template Juna.Chimp for spatial registration and the macro-anatomical brain parcellation Davi130 for standardized whole-brain analysis. Additionally, we introduce a ready-to-use image processing pipeline built upon the CAT12 toolbox in SPM12, implementing a standard human image preprocessing framework in chimpanzees. Applying this approach to data from 178 subjects, we find strong evidence for age-related GM atrophy in multiple regions of the chimpanzee brain, as well as, a human-like anterior-posterior pattern of hemispheric asymmetry in medial chimpanzee brain regions.

Introduction

Chimpanzees (*Pan troglodytes*) along with bonobos (*Pan paniscus*) represent the closest extant relatives of humans sharing a common ancestor approximately 7-8 million years ago (Langergraber et al. 2012). Experimental and observational studies, in both the field and in captivity, have documented a range of cognitive abilities that are shared with humans such as tool use and manufacturing (Shumaker et al. 2011), symbolic thought (de Waal 1996), mirror self-recognition (Anderson and Gallup 2015; Hecht et al. 2017) and some basic elements of language (Savage-Rumbaugh 1986; Savage-Rumbaugh and Lewin 1994; Tomasello and Call 1997) like conceptual metaphorical mapping (Dahl and Adachi 2013). This cognitive complexity together with similar neuroanatomical features (Zilles et al. 1989; Rilling and Insel 1999; Gomez-Robles et al. 2013; Hopkins et al. 2014a, 2017) and genetic proximity (Waterson et al. 2005) renders these species unique among non-human primates to study the evolutional origins of the human condition. In view of evolutionary neurobiology, the relatively recent divergence between humans and chimpanzees explains the striking similarities in major gyri and sulci, despite profound differences in overall brain size. Numerous studies using magnetic resonance imaging (MRI) have compared relative brain size, shape, and gyrification in humans and chimpanzees (Zilles et al. 1989; Rilling and Insel 1999; Gomez-Robles et al. 2013; Hopkins et al. 2014b, 2017).

Previous studies of brain aging in chimpanzees have reported minimal indications of atrophy (Herndon et al. 1999; Sherwood et al. 2011; Chen et al. 2013; Autrey et al. 2014). Nevertheless, Edler and colleagues (2017) recently found that brains of older chimpanzees' exhibit both neurofibrillary tangles and amyloid plaques, the classical features of Alzheimer's disease (AD). Neurodegeneration in the aging human brain includes marked atrophy in frontal and temporal lobes and decline in glucose metabolism even in the absence of detectable amyloid beta deposition, which increases the likelihood of cognitive decline and development of AD (Jagust 2018). Given the strong association of brain atrophy and amyloid beta in humans, this phenomenon requires further investigation in chimpanzees.

Cortical asymmetry is a prominent feature of brain organization in many primate species (Hopkins et al. 2015) and was recently shown in humans in a large scale ENIGMA (Enhancing Neuroimaging Genetics through Meta-Analysis) study (Kong et al. 2018). For chimpanzees, various studies have reported population-level asymmetries in different parts of the brain associated with higher order cognitive functions like tool-use (Freeman et al. 2004; Hopkins et al. 2008, 2017; Hopkins and Nir 2010; Lyn et al. 2011; Bogart et al. 2012; Gilissen and Hopkins 2013) but these results are difficult to compare within and across species, due to the lack of standardized registration and parcellation techniques as found for humans.

To date, there is no common reference space for the chimpanzee brain available to reliably associate and quantitatively compare neuro-anatomical evidence, nor is there a standardized image processing protocol for T1-weighted brain images from chimpanzees that matches human imaging standards. With the introduction of voxel-based morphometry (VBM, Ashburner and Friston 2000) and the ICBM (international consortium of brain mapping) standard human reference brain templates almost two decades ago (Mazziotta et al. 2001) MRI analyses became directly comparable and generally reproducible In this study we adapt state-of-the-art MRI (magnetic resonance imaging) processing methods to assess brain aging and cortical asymmetry in the chimpanzee brain. To make this possible, we rely on the largest openly available resource of chimpanzee MRI data: the *National Chimpanzee Brain Resource* (NCBR, www.chimpanzeebrain.org), including *in vivo* MRI images of 223 subjects from 9 to 54 years of age (Mean age = 26.9 ± 10.2 years). The aim of this study is the creation of a chimpanzee template permitting automated and reproducible image registration, normalization, statistical analysis and visualization to systematically investigate brain aging and hemispheric asymmetry in chimpanzees.

Results

Initially, we created the population based Juna (Forschungszentrum Juelich - University Jena) T1-template, tissue probability maps (TPM) for tissue classification and a non-linear spatial registration 'Shooting' templates (Figure 1) in an iterative fashion at 1mm spatial resolution. The preprocessing pipeline and templates creation were established using the freely available *Statistical Parametric Mapping* (SPM12 v7487, http://www.fil.ion.ucl.ac.uk/spm/) software and *Computational Anatomy Toolbox* (CAT12 r1434, http://www.neuro.uni-jena.de/cat/). Juna.Chimp templates and the Davi130 parcellation as well as images for analysis are interactively accessible via the Juna.Chimp web viewer (http://junachimp.inm7.de/).

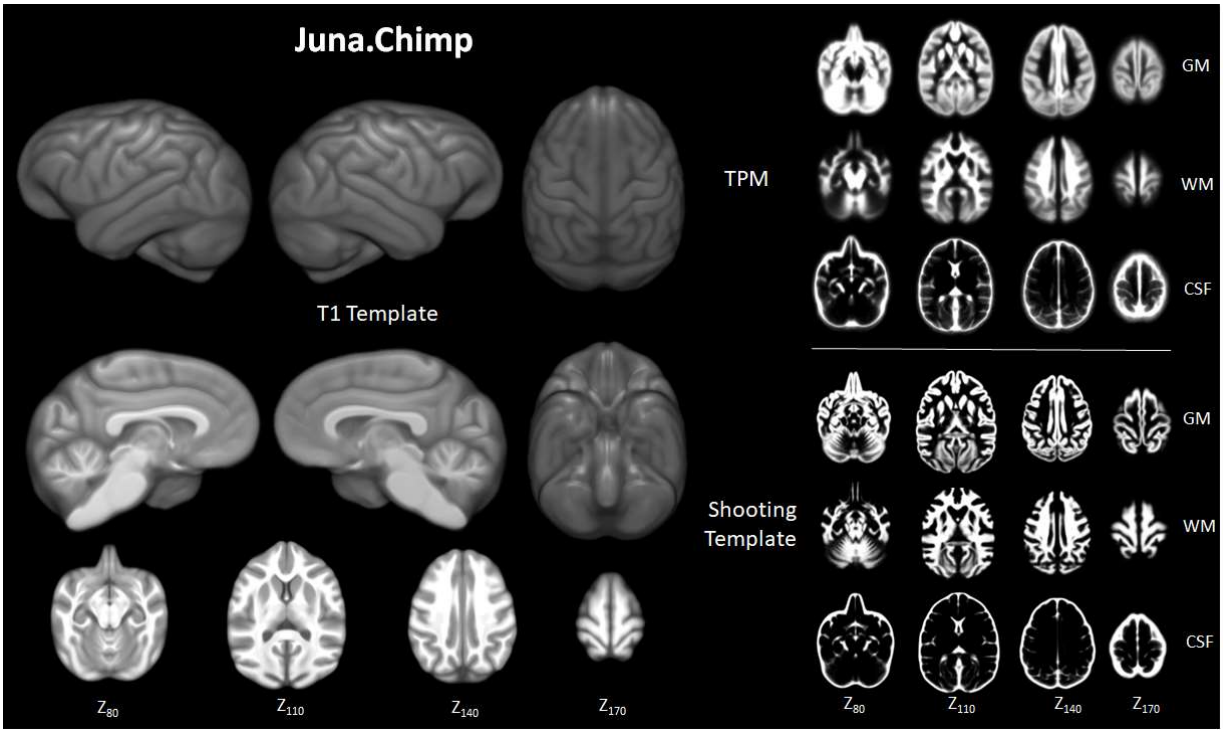

Figure 1. Juna.Chimp templates including the average T1- template, tissue probability maps (TPM), and Geodesic Shooting template. For Shooting templates and TPM axial slices are shown of gray matter (GM), white matter (WM), and cerebrospinal fluid (CSF). All templates are presented at 0.5mm resolution.

To enable more direct comparison to previous research, we manually created the Davi130 parcellation (by R.D. and S.V.), a whole brain macroanatomical annotation

based on the Juna T1 template (Figure 2). The delineation of regions within the cortex was determined by following major gyri and sulci, whereby, large regions were arbitrarily split into two to three sub-regions of approximate equal size even though histological studies show that micro-anatomical borders between brain regions are rarely situated at the fundus (Sherwood et al. 2003; Schenker et al. 2010; Spocter et al. 2010; Amunts and Zilles 2015).. This process yielded 65 regions per hemisphere for a total of 130 regions for the Davi130 macro-anatomical manual parcellation (Figure 2, Supplementary Table 1).

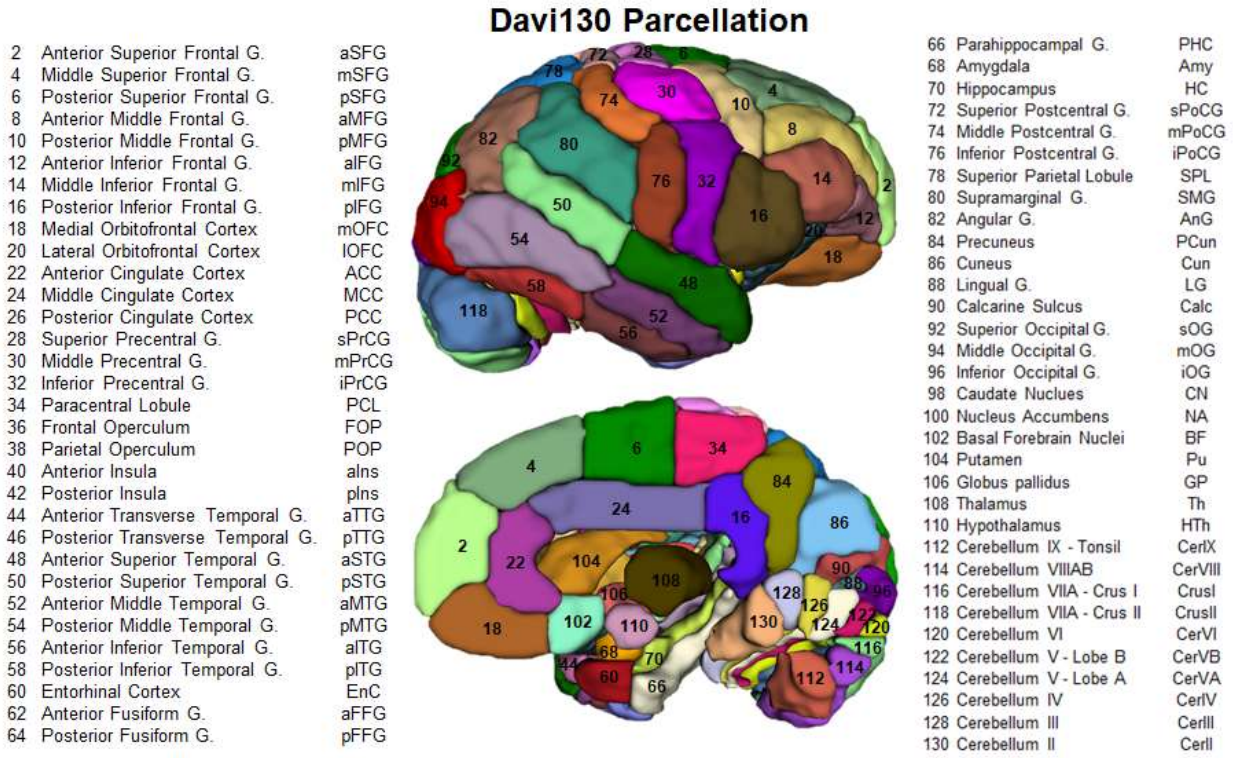

Figure 2. Lateral and medial aspect of the Davi130 parcellation right hemisphere. Visible regions are numbered with Davi130 parcellation region numbers and correspond to names in the figure. Odd numbers correspond to left hemisphere regions while even numbers are in the right hemisphere.

Following successful CAT12 preprocessing rigorous quality control (QC) was employed to identify individual MRI scans suitable for statistical analysis of brain aging and hemispheric asymmetry in chimpanzees. Our final sample consists of 178 chimpanzees

including 120 females with an age range of 11 to 54 years and a mean age of 26.7 ± 9.8 years (Figure 3A). Correlation analysis between GM fraction of total intracranial volume and age revealed a significant negative association between the two (R^2 = 0.11, p < 0.0001) demonstrating age-related decline in overall GM (Figure 3B). Both male and female subjects show a significant age effect on GM (male: R^2 = 0.08, p = 0.03; female R^2 = 0.11, p = 0.0001). The linear model showed no significant sex differences of GM decline (p = 0.08).

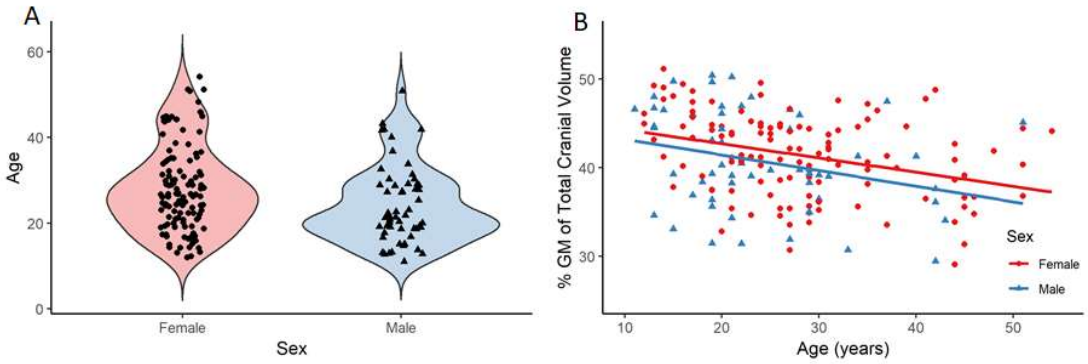

Figure 3. A - Distribution of age and sex in the final sample of 178 chimpanzees. B- linear relationship between GM and age for female and male respectively.

Region based morphometry analysis was applied to test for local effect of age on GM. Linear regression analyses identified 23 regions in the Davi130 parcellation across both hemispheres that were significantly associated with age after family-wise error (FWE) correction for multiple testing (Figure 4, for all region results see Supplementary). Specifically, GM decline with age was found bilaterally in the lateral orbitofrontal cortex (lOFC) and mid-cingulate (MCC) as well as unilaterally in the right precuneus (PCun), posterior cingulate (PCC), and lingual gyrus (LG), in addition to the left middle superior frontal gyrus(mSFG), anterior transverse temporal gyrus (aTTG) and calcarine sulcus (Calc) within the cerebral cortex. The strongest association with aging was in the bilateral putamen (Pu) and caudate nucleus (CN), while the nucleus accumbens (NA) and superior cerebellum (CerIII, CerIV, CerVA, and right CrusII) also presented a significant aging effect. Finally, to test for more fine grained effects of aging, the same sample was analyzed with VBM revealing additional clusters of GM that are significantly affected by age in chimpanzees (Figure 5) after FWE correction using threshold-free cluster enhancement (TFCE) (Smith and

Nichols 2009). On top of the regions identified by region-wise morphometry, we found voxel-wise effects throughout anterior cingulate cortex (ACC), middle frontal gyrus (MFG) and in parts of the superior and inferior frontal gyrus (SFG, IFG), postcentral gyrus, superior and transverse temporal gyrus (STG, TTG), angular gyrus (AnG), superior occipital gyrus (sOG) and in inferior parts of the cerebellum.

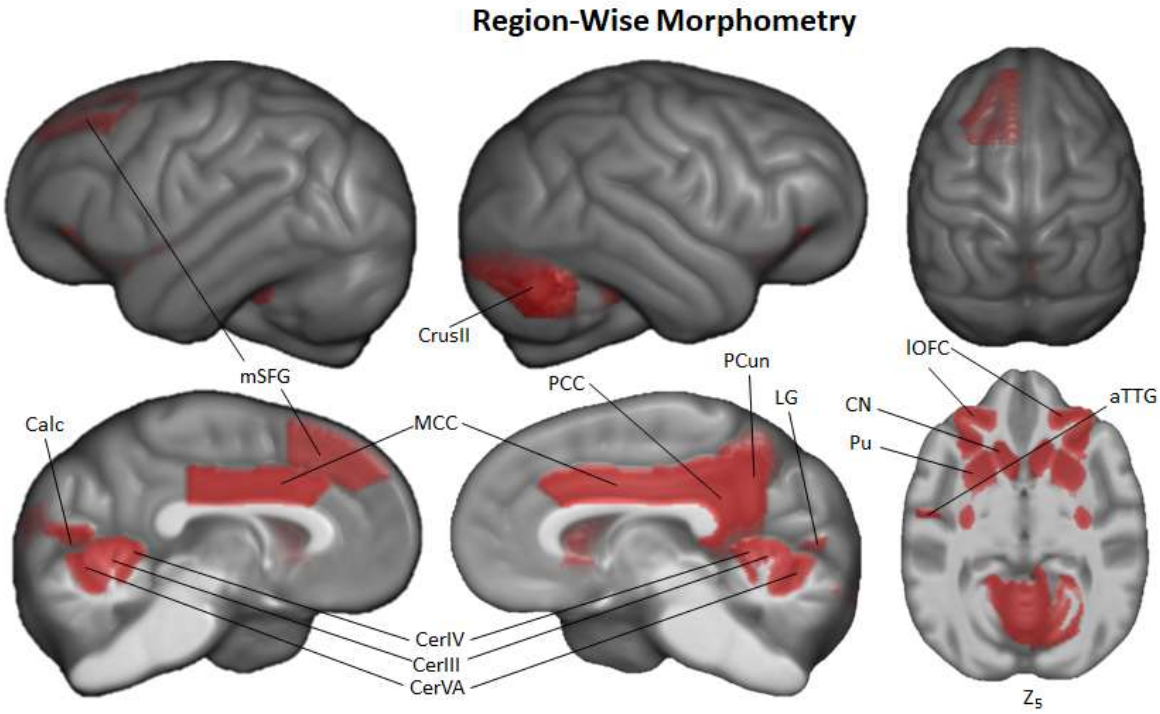

Figure 4. Region-wise morphometry in the Davi130 parcellation age regression where red regions represent Davi130 regions that remained significant at $p \leq 0.05$ following FWE correction. aTTG – anterior transverse temporal gyrus, Calc – Calcarine sulcus, CrusII – cerebellum VIIA-CrusII, CerVA – cerebellum VA, CerIV – cerebellum IV, CerIII – cerebellum III, CN – caudate nucleus, lOFC – lateral orbitofrontal cortex, LG – lingual gyrus, MCC – medial cingulate cortex, mSFG – middle superior frontal gyrus, PCC – posterior cingulate cortex, PCun – precuneus, Pu – putamen.

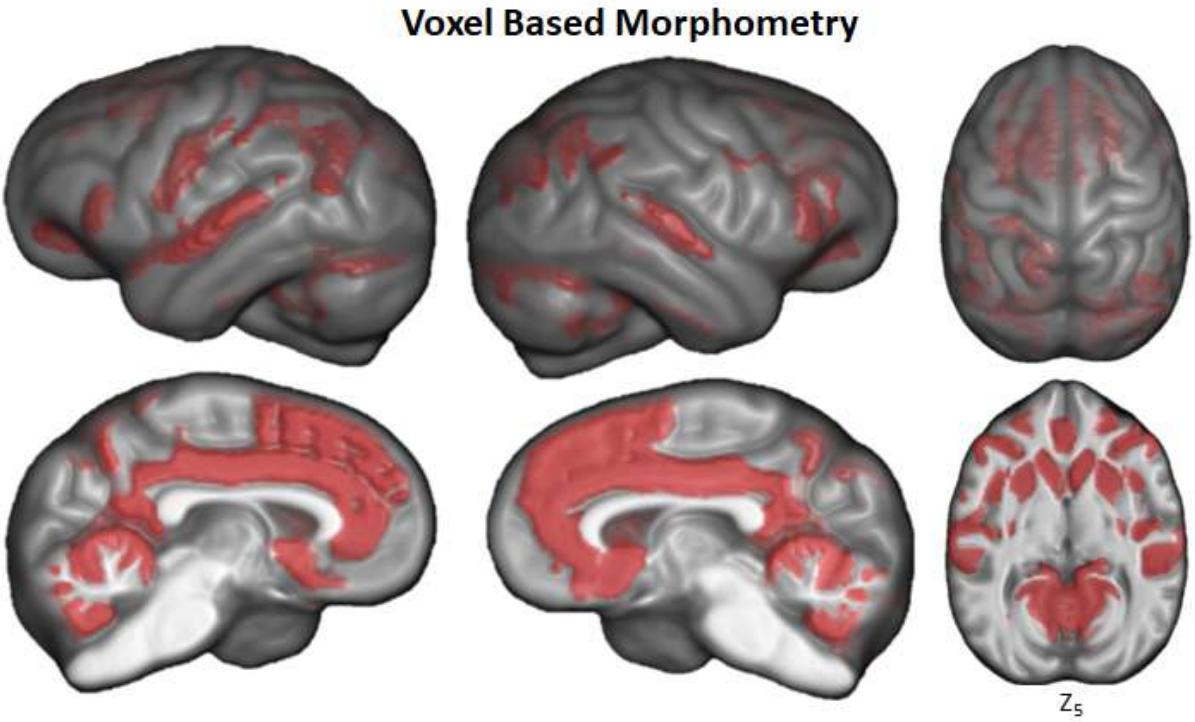

Figure 5. Voxel based morphometry of aging on GM volume using TFCE with FWE correction at $p \leq 0.05$.

Hemispheric asymmetry of the chimpanzee brain was assessed for each cortical Davi130 region with a total of 29 macro-anatomical regions exhibiting significant cortical asymmetry after FWE correction (Figure 6, all region asymmetry found in Supplementary). Slightly more regions were found with greater GM volume on the right hemisphere (n=17) as compared to the left (n=12). In the left hemisphere, we found more GM laterally in the inferior postcentral gyrus (iPoCG), supramarginal gyrus (SMG) and superior occipital gyrus (sOG), insula and posterior TTG as well as medially in the orbitofrontal cortex (mOFG), basal forebrain nuclei (BF), hippocampus (HC), and anterior SFG. Rightward cortical asymmetry was located medially in the paracentral lobule (PCL), PCC, cuneus (Cun) and the region surrounding the calcarine sulcus, in the parahippocampal gyrus (PHC) and posterior fusiform gyrus (pFFG), as well as in the parietal operculum (POP). Laterally, rightward cortical asymmetry was found in the middle postcentral gyrus (mPoCG) and posterior superior temporal gyrus (pSTG). Within the basal ganglia, leftward GM asymmetry was observed in the putamen (Pu) while, rightward asymmetry is in the globus pallidus (GP) and thalamus (Th). In the anterior cerebellar lobe, there was

leftward (CerIV) and rightward (CerII) GM asymmetry. The posterior cerebellum showed only rightward (CerVI, CerVB, and CerIX) asymmetry.

The moderate pattern of asymmetry we observed medially was a shift from more anterior regions showing leftward GM asymmetry (mOFC, BF, and aSFG) while more posterior regions presented rightward asymmetry (PCL, PCC, Cun, Calc, and LG). The lateral regions did not show a decipherable pattern.

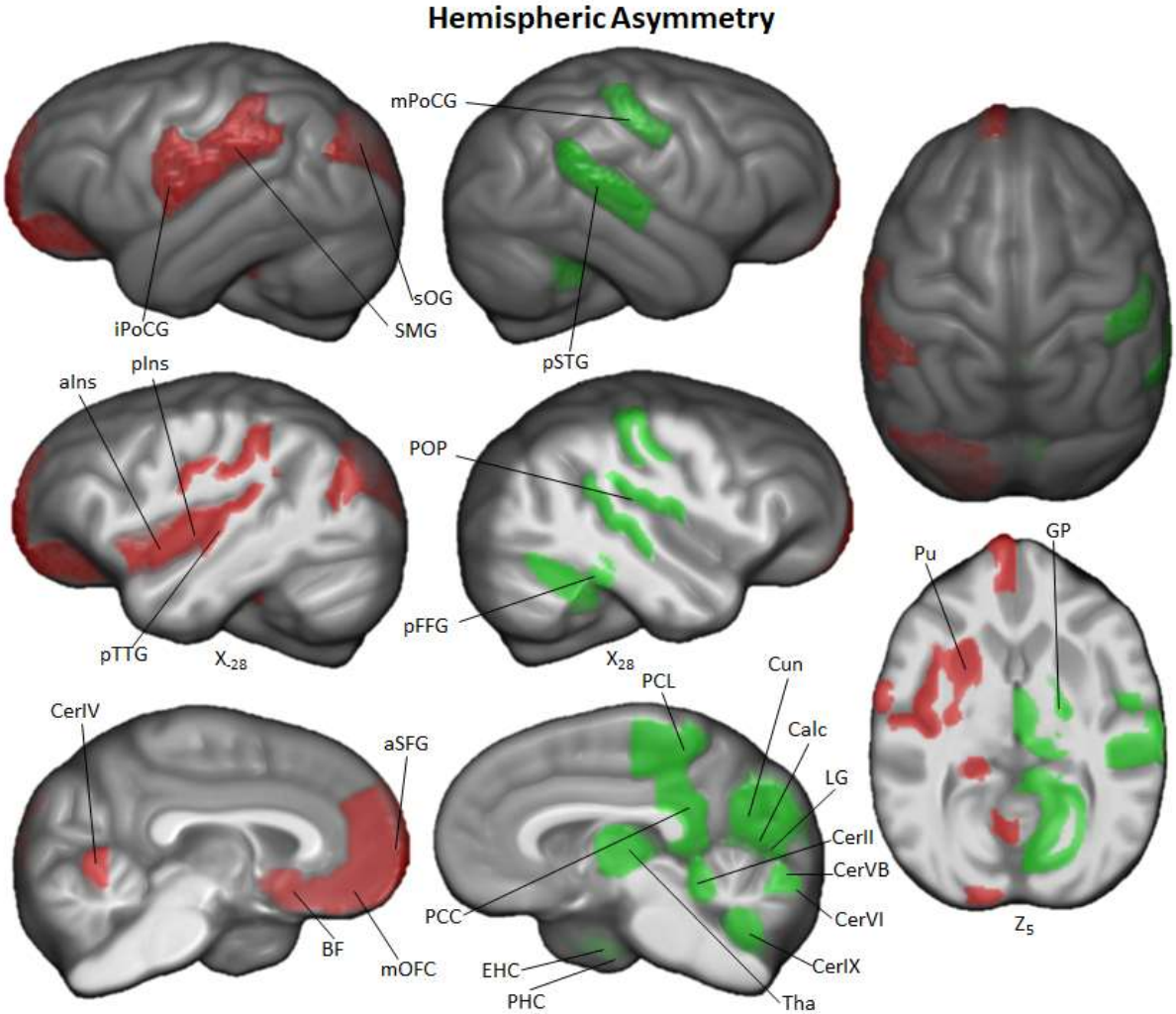

Figure 6. Hemispheric asymmetry of Davi130 regions within the chimpanzee sample. Significant leftward (red) and rightward (green) asymmetrical regions are those with a $p \leq 0.05$ after FWE correction. aIns – anterior insula, aSFG – anterior superior frontal gyrus, BF – basal forebrain

nuclei, Calc – calcarine sulcus, CerIX – cerebellum IX, CerVB – cerebellum V anterior B, CerVI – cerebellum VI, CerIV – cerebellum IV, CerII, cerebellum II, Cun – cuneus, EnC – entorhinal cortex, GP – globus pallidus, iPoCG – inferior postcentral gyrus, LG – lingual gyrus, mOFC – medial orbitofrontal cortex, mPoCG – middle postcentral gyrus, PCC – posterior cingulate cortex, PCL – paracentral lobule, pFFG – posterior fusiform gyrus, PHC – parahippocampal gyrus, pIns – posterior insula, POP – parietal operculum, pSTG – posterior superior temporal gyrus, pTTG – posterior transverse temporal gyrus, Pu – putamen, SMG – supramarginal gyrus, sOG – superior occipital gyrus, Th – thalamus. The hippocampus (HC) is significantly leftward lateralized but is not shown in this figure.

Discussion

As a common reference space for the analysis of chimpanzee brain data, we created the Juna.Chimp template, constructed from a large heterogeneous sample of T1-weighted MRI's from the NCBR. The Juna.Chimp template includes a reference T1-template, along with probability maps of brain and head tissues accompanied by a Geodesic Shooting template for the publicly available SPM12/CAT12 preprocessing pipeline to efficiently segment and spatially normalize individual chimpanzee T1 images. The T1-template and TPM can be also used as the target for image registration with other popular software packages, such as FSL (https://fsl.fmrib.ox.ac.uk/fsl) or ANTs (http://stnava.github.io/ANTs/).

Additionally, we provide the manually segmented, macro-anatomical Davi130 whole-brain parcellation comprising 130 cortical, sub-cortical and cerebellar brain regions, which enables systematical extraction of volumes-of-interest from chimpanzee MRI data. The image processing pipeline and Davi130 parcellation were used to investigate ageing and interhemispheric asymmetry in the chimpanzee brain. Our analyses demonstrated strong age-related GM atrophy as well as marked hemispheric asymmetry over the whole cortex.

We found clear evidence of global and local GM decline in the aging chimpanzee brain even though previous research into age-related changes in chimpanzee brain organization has shown little to no effect (Herndon et al. 1999; Sherwood et al. 2011; Chen

et al. 2013; Autrey et al. 2014). This can be attributed on the one hand to the larger number of MRI scans available via the NCBR including 30% of older subjects with 55 individuals over 30 and 12 over 45 years of age, which is crucial for modelling the effect of aging (Chen et al. 2013; Autrey et al. 2014). On the other hand, state-of-the-art image processing enabled the creation of the species specific Juna.Chimp templates, which largely improves tissue segmentation and registration accuracy (Ashburner and Friston 2000). Non-linear registration was also improved by the large heterogeneous sample utilized for the creation of the templates encompassing a representative amount of inter-individual variation. We used the well-established structural brain imaging toolbox CAT12 to build a reusable chimpanzee preprocessing pipeline catered towards analyzing local tissue-specific anatomical variations as measured with T1 weighted MRI. The Davi130-based region-wise and the voxel-wise morphometry analysis consistently showed localized GM decline in lOFC, the basal ganglia, MCC, PCC, PCun and superior cerebellum. The VBM approach additionally produced evidence for age effects in bilateral prefrontal cortex, ACC, superior temporal regions and throughout the cerebellum. These additional effects can be expected, as VBM is more sensitive to GM changes due to aging (Kennedy et al. 2009). The brain regions revealing GM decline in both approaches in particular medial and temporal cortical regions and the basal ganglia have also been shown to exhibit GM atrophy during healthy aging in humans (Good et al. 2001b; Kennedy et al. 2009; Crivello et al. 2014; Minkova et al. 2017).

Very recently, it has been shown that stress hormone levels increase with age in chimpanzees, a process previously thought to only occur in humans which can cause GM volume decline (Emery Thompson et al. 2020). This further strengthens the argument that age-related GM decline is also shared by humans closest relative, the chimpanzee. Furthermore, Edler et al. (2017) found Alzheimer's disease-like accumulation of amyloid beta plaques and neurofibrillary tangles located predominantly in prefrontal and temporal cortices in a sample of elderly chimpanzees between 37 and 62 years of age. As the aggregation of these proteins is associated with localized neuronal loss and cortical atrophy in humans (La Joie et al. 2012; Llado et al. 2018), the age-related decline in GM volume shown here is well in line with the findings by Jagust (2016) associating GM atrophy with

amyloid beta. These findings provide a biological mechanism for accelerated GM decrease in prefrontal, limbic, and temporal cortices in chimpanzees. In contrast, elderly rhesus monkeys show GM volume decline without the presence of neurofibrillary tangles (Alexander et al. 2008; Shamy et al. 2011). Taken together, regionally specific GM atrophy seems to be a common aspect of the primate brain aging pattern observed in macaque monkeys, chimpanzees and humans. Yet, to make a case for the existence of Alzheimer's disease in chimpanzees, validated cognitive tests for Alzheimer's-like cognitive decline in non-human primates are needed, to test for direct associations between cognitive decline with tau pathology and brain atrophy.

Hemispheric asymmetry was found in almost two-thirds of all regions of the Davi130 parcellation, reproducing several regional findings reported in previous studies using diverse image processing methods as well as uncovering numerous novel population-level asymmetries. Previous studies utilizing a region-wise approach based on hand-drawn or atlas derived regions also reported leftward asymmetry of volume of the planum temporale (PT) (Lyn et al. 2011; Gilissen and Hopkins 2013), and of cortical thickness in STG (Hopkins and Avants 2013), and the insula (Hopkins et al. 2017). Region-wise morphometry also demonstrated rightward asymmetry in thickness of the PCL and PHC (Hopkins et al. 2017). Previous VBM findings also revealed leftward asymmetry in the anterior SFG and SMG along with rightward lateralization of the posterior SFG, and middle part of the PoCG (Hopkins et al. 2008). In the current study, new regions of larger GM volume in the left hemisphere were found in frontal (mSFG, mOFC), limbic (HC), temporal (aTTG), and parietal (iPoCG) cortices as well as in the basal ganglia (BF, Pu) and cerebellum (CerIV). Novel rightward asymmetries could also be seen in temporal (pFFG), limbic (PCC, EnG), parietal (POP), and occipital (Cun, LG, Calc) cortices besides the basal ganglia (Th, GP) and the cerebellum (CerIX, CerVI, CerVB, CerII).

Significant leftward asymmetries in Davi130s' region pTTG which contains the PT, is consistent with previous studies in GM volume of the PT, its surface area (Hopkins and Nir 2010), and cytoarchitecture (Zilles et al. 1996; Gannon et al. 1998; Spocter et al. 2010). At this cortical location, old world monkeys lack the morphological features of the

PT, nevertheless several species have been shown to display asymmetry in Sylvian fissure length (Lyn et al. 2011; Marie et al. 2018).

Interestingly, the parietal operculum showed rightward asymmetry, while Gilissen and Hopkins (2013) showed that the left parietal operculum was significantly longer in chimpanzees, compared to the right. The left lateral sulcus in the Juna.Chimp template appears to proceed further posteriorly and superiorly compared to the right, confirming this finding, even though we found greater GM volume in the right POP as compared to the left.

Population-level asymmetries in the pIFG in chimpanzees were documented almost two decades ago by Cantalupo and Hopkins (2001), who reported a leftward asymmetry in pIFG volume in a small sample of great apes. In subsequent studies this result could not be replicated when considering GM volume (Hopkins et al. 2008; Keller et al. 2009) or cytoarchitecture (Schenker et al. 2010). We also failed to find a leftward asymmetry in GM volume for the pIFG, in contrary to asymmetries found in humans (Amunts et al. 1999; Uylings et al. 2006; Keller et al. 2009). The prominent leftward PT asymmetry in chimpanzees is also a well-documented population-level asymmetry in humans (Good et al. 2001a; Watkins 2001). The overall regional distribution of asymmetry in chimpanzees is partially similar to that found in human cortical organization (Good et al. 2001a; Luders et al. 2006; Zhou et al. 2013; Koelkebeck et al. 2014; Plessen et al. 2014; Chiarello et al. 2016; Maingault et al. 2016; Kong et al. 2018).

Gross hemispheric asymmetry in humans follows a general structure of frontal rightward and occipital leftward asymmetry known as the ‘Yakovlevian torque’. This refers to the bending of the anterior right hemisphere over the midline into the left and the posterior left hemisphere bending over to the right and is represented as differences in widths of frontal and occipital lobes (Toga and Thompson 2003). This organizational trait was apparent in the Juna.Chimp templates with a slight frontal and occipital bending, which was manually adapted when labelling the medial Davi130 regions. The higher leftward GM density in frontal regions and rightward asymmetry in occipital regions may also follow this trend. Of note, this organizational pattern of asymmetry was less apparent in lateral

333 cortical structures, however medially, this anterior-posterior asymmetry is evident in chim-
334 panzees, challenging recent findings from Li and colleagues (2018) who rejected the 'Ya-
335 kovlevian torque' in chimpanzees. Specifically, leftward asymmetry of the frontal regions
336 aSFG, BF, and mOFC and the rightward asymmetry of posterior regions PCL, PCC, Cun,
337 Calc, and LG aligns with the pattern of asymmetry reported in human cortical GM volume,
338 thickness and surface area (Luders et al. 2006; Zhou et al. 2013; Plessen et al. 2014;
339 Chiarello et al. 2016; Kong et al. 2018).

340 The NCBR offers the largest and richest openly available dataset of chimpanzee
341 brain MRI scans acquired over a decade with 1.5T and 3T MRI at two locations, capturing
342 valuable inter-individual variation in one large heterogeneous sample. To account for the
343 scanner effect on GM estimation, field strength was modelled as a covariate of no interest
344 for analyzing the age effect on GM volume. Rearing has been shown to affect GM struc-
345 tural covariance networks and cortical organization (Bogart et al. 2014; Bard and Hopkins
346 2018) while handedness has been shown to correlate with asymmetry in the motor cortex
347 (Hopkins and Cantalupo 2004) and the volume of IFG (Taglialatela et al. 2006) as well as
348 with gyrification asymmetry (Hopkins et al. 2007). Therefore, these covariates may also
349 modulate hemispheric asymmetry and/or age-related GM volume decline here, but as
350 these data were not available for all subjects, we did not consider these effects in order
351 to include as many subjects as possible to model effects of age. The focus of this study
352 was the analysis of GM volume, even though the CAT12 image processing pipeline in-
353 cludes surface projection and analysis. Consequently, the next step will be the application
354 of CAT12 to analyze cortical surface area, curvature, gyrification, and thickness of the
355 chimpanzee brain, to include behavioral data and the quantitative comparison to humans
356 and other species, as cortical surface projection permits a direct inter-species comparison
357 due to cross species registration.
358

359 **Conclusion**

360 In conclusion, we present the new chimpanzee reference template Juna.Chimp,
361 TPM's, the Davi130 whole brain parcellation, and the CAT12 preprocessing pipeline
362 which is ready-to-use by the wider neuroimaging community. Investigations of age-related

363 GM changes in chimpanzees using both region-wise and voxel-based morphometry,
364 showed a substantial age effect, providing further evidence for human like physiological
365 aging processes in chimpanzees. Examining population based cortical asymmetry in
366 chimpanzees yielded further evidence for the well-documented lateralization of PT. Addi-
367 tionally, an anterior-posterior left-right pattern of asymmetry as observed in humans was
368 found predominantly in medial regions of the chimpanzee cortex.

369

370 **Materials and Methods**

371 Subject Information and Image Collection Procedure

372 This study analyzed structural T1-weighted MRI scans of 223 chimpanzees (137
373 females; 9 - 54 y/o, mean age 26.9 ± 10.2 years) from the NCBR (www.chimpanzee-
374 brain.org). The chimpanzees were housed at two locations including, the *National Center*
375 *for Chimpanzee Care* of *The University of Texas MD Anderson Cancer Center* (UT-
376 MDACC) and the *Yerkes National Primate Research Center* (YNPRC) of Emory Univer-
377 sity. The standard MR imaging procedures for chimpanzees at the YNPRC and UT-
378 MDACC are designed to minimize stress for the subjects. For an in-depth explanation of
379 the imaging procedure please refer to Autrey et al. (2014). Seventy-six chimpanzees were
380 scanned with a Siemens Trio 3 Tesla scanner (Siemens Medical Solutions USA, Inc.,
381 Malvern, Pennsylvania, USA). Most T1-weighted images were collected using a three-
382 dimensional gradient echo sequence with 0.6 × 0.6 × 0.6 resolution (pulse repetition =
383 2300 ms, echo time = 4.4 ms, number of signals averaged = 3). The remaining 147 chim-
384 panzees were scanned using a 1.5T GE echo-speed Horizon LX MR scanner (GE Medi-
385 cal Systems, Milwaukee, WI), predominantly applying gradient echo sequence with 0.7 ×
386 0.7 × 1.2 resolution (pulse repetition = 19.0 ms, echo time = 8.5 ms, number of signals
387 averaged = 8).

388 Creation of Chimpanzee Templates

389 An iterative process as by Franke et al. (2017) was employed to create the
390 Juna.Chimp template, with T1 average, Shooting registration template (Ashburner and

Friston 2011), as well as the TPM (Figure 7). Initially, a first-generation template was produced using the “greater_ape” template delivered by CAT (Dahnke and Gaser 2017; Gaser et al. 2020) that utilizes data provided in Rilling and Insel (1999). The final segmentation takes the bias-corrected, intensity-normalized, and skull-stripped image together with the initial SPM-segmentation to conduct an Adaptive Maximum A Posterior (AMAP) estimation (Rajapakse et al. 1997) with a partial volume model for sub-voxel accuracy (Tohka et al. 2004). The affine normalized tissue segments of GM, WM, and CSF were used to create a new Shooting template that consists of four major non-linear normalization steps allowing to normalize new scans. To create a chimpanzee-specific TPM, we average the different Shooting template steps to benefit from the high spatial resolution of the final Shooting steps but also include the general affine aspects to avoid over-optimization. Besides the brain tissues the TPM also included two head tissues (bones and muscles) and a background class for standard SPM12 (Ashburner and Friston 2005) and CAT12 preprocessing. The internal CAT atlas was written for each subject and mapped to the new chimpanzee template using the information from the Shooting registration. The CAT atlas maps were averaged by a median filter and finally manually corrected. This initial template was then used in the second iteration of CAT segmentation to establish the final chimpanzee-specific Juna.Chimp template, which was imported into the standard CAT12 preprocessing pipeline to create the final data used for the aging and asymmetry analyses.

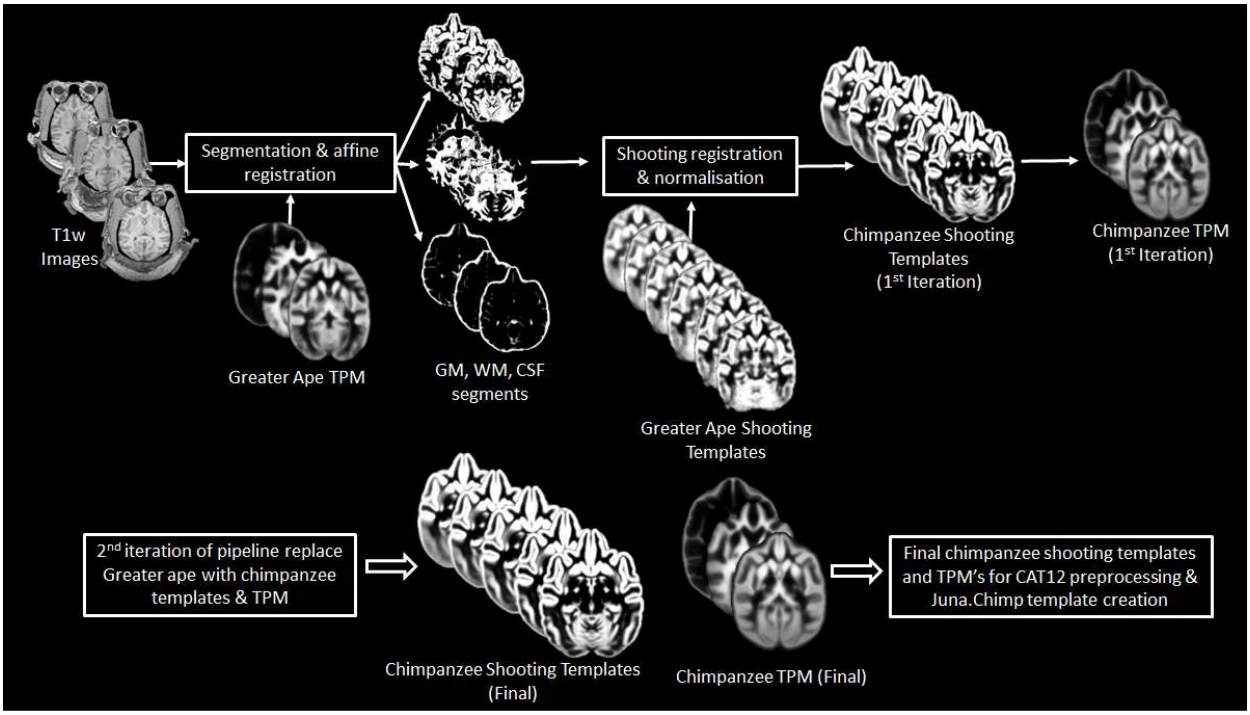

Figure 7. Workflow for creation of chimpanzee specific Shooting template and TPM, which can then be used in CAT12 structural preprocessing pipeline to create the Juna.Chimp template.

The resulting chimpanzee-Shooting template, TPM and CAT atlas establishes the robust and reliable base to segment and spatially normalize the T1-weighted images utilizing CAT12's processing pipeline (Dahnke and Gaser 2017; Gaser et al. 2020).

Davi130 parcellation

The average T1 and final Shooting template were used for a manual delineation of macro-anatomical GM structures. Identification and annotation of major brain regions were performed manually using the program, 3D Slicer 4.10.1 (https://www.slicer.org). The labeling enables automated, region-based analysis of the entire chimpanzee brain and allows for robust statistical analysis. Nomenclature and location of regions were ascertained by consulting both chimpanzee and human brain atlases (Bailey P, Bonin GV 1950; Mai et al. 2015). The labelling was completed by two authors (S.V. & R.D.) and reviewed by two experts of chimpanzee brain anatomy (C.C.S. & W.D.H.).

A total of 65 GM structures within the cerebrum and cerebellum of the left hemisphere were annotated and then flipped to the right hemisphere. The flipped annotations

429 were then manually adapted to the morphology of the right hemisphere to have complete
430 coverage of the chimpanzee brain with 130 labels. The slight bending of the anterior part
431 of the right hemisphere and the posterior part of the left hemisphere over the midline
432 observed in our template and annotated within our Davi130 labelling, does not align with
433 previous findings claiming that this morphological trait is specific to the human brain (Li
434 et al. 2018; Xiang et al. 2019).

435 The location of macroscopic brain regions was determined based on major gyri of
436 the cerebral cortex, as well as distinct anatomical landmarks of the cerebellar cortex, and
437 basal ganglia. Of note, the border between two gyri was arbitrarily set as the mid-point of
438 the connecting sulcus. Large gyri were further subdivided into two or three parts based
439 on their size and structural features, such as sulcal fundi and gyral peaks, to enable
440 greater spatial resolution and better inter-regional comparison. Naming of subdivisions
441 was based entirely on spatial location, e.g., anterior, middle, posterior, and do not claim
442 to correspond to functional parcellations.

443 Quality Control

444 Rigorous QC was employed on all images using two iterative steps. The first step
445 utilized the built-in CAT12 quality assurance and 'check sample homogeneity' function.
446 The modulated GM maps were initially tested for sample in-homogeneity for each scanner
447 strength separately (1.5T and 3T). The images that passed the first QC step went through
448 a final round of sample inhomogeneity testing as a whole sample to finally arrive at our
449 study sample, which included 178 chimpanzees (120 females, 11 – 54 years old, mean
450 = 26.7 ± 9.8). A more in-depth explanation of the QC procedure can be found in Supple-
451 mentary 1.2.

452 Age-Related Changes in Total Gray Matter

453 A linear regression model was used to determine the effect of aging on total GM
454 volume. Firstly, total GM volume for each subject was converted into a percentage of total
455 intracranial volume (TIV) to account for the variation in head size. This was then entered

456 into a linear regression model as the dependent variable with age and sex as the inde-
457 pendents. Sex-specific models were conducted with males and females separately using
458 age as the only dependent variable. The slope of each regression line was determined
459 using R^2 and a p-value of $p \leq 0.05$ was used to determine the significant effect of age and
460 sex on total GM volume.

461 Age-Related Changes in Gray Matter Using Davi130 Parcellation

462 The Davi130 parcellation was applied to the modulated GM maps to conduct re-
463 gion-wise morphometry analysis. First, the Davi130 regions were masked with a 0.1 GM
464 mask to remove all non-GM portions of the regions. Subsequently, the average GM in-
465 tensity of each region for all QC-passed chimpanzees was calculated. A multiple regres-
466 sion model was conducted for the labels from both hemispheres, whereby, the dependent
467 variable was GM volume and the predictor variables were age, sex, TIV, and scanner.
468 Significant age-related GM decline was established for a Davi130 label with a $p \leq 0.05$,
469 after correcting for multiple comparisons using FWE (Holm 1979).

470 Voxel-Based Morphometry

471 VBM analysis was conducted using CAT12 to determine the effect of aging on
472 local GM volume. The modulated and spatially normalized GM segments from each sub-
473 ject were spatially smoothed with a 4 mm FWHM (full width half maximum) kernel prior to
474 analyses. To restrict the overall volume of interest, an implicit 0.4 GM mask was em-
475 ployed. As MRI field strength is known to influence image quality, and consequently, tis-
476 sue classification, we included scanner strength in our VBM model as a covariate. The
477 dependent variable in the model was age, with covariates of TIV, sex, and scanner. The
478 VBM model was corrected for multiple comparisons using TFCE with 5000 permutations
479 (Smith and Nichols 2009). Significant clusters were determined at $p \leq 0.05$, after correct-
480 ing for multiple comparisons using FWE.

481 Hemispheric Asymmetry

482 As for the age regression analysis, all Davi130 parcels were masked with a 0.1
483 GM mask to remove non-GM portions within regions. Cortical hemispheric asymmetry of

Davi130 labels was determined using the formula *Asym = (L - R) / (L + R) * 0.5* (Kurth et al. 2015; Hopkins et al. 2017), whereby L and R represent the average GM volume for each region in the left and right hemisphere, respectively. Therefore, the bi-hemispheric Davi130 regions were converted into single *Asym* labels (n=65) with positive *Asym* values indicating a leftward asymmetry, and negative values, a rightward bias. One-sample *t*-tests were conducted for each region under the null hypothesis of *Asym = 0*, and significant leftward or rightward asymmetry was determined with a $p \leq 0.05$, after correcting for multiple comparisons using FWE (Holm 1979).

Exemplar Pipeline Workflow

To illustrate the structural processing pipeline, we have created exemplar MATLAB SPM batch scripts that utilizes the Juna.Chimp templates in CAT12's preprocessing workflow to conduct segmentation, spatial registration, and finally some basic age analysis on an openly available direct-to-download chimpanzee sample (http://www.chimpanzee-brain.org/mri-datasets-for-direct-download). These scripts require the appropriate templates which can be downloaded from the Juna.Chimp web viewer (SPM/CAT_templates.zip) and then place the templates_animals/ folder into the latest version CAT12 Toolbox directory (CAT12.7 r1609). The processing parameters are similar to those conducted in this study, although different DICOM conversions and denoising were conducted. Further information regarding each parameter can be viewed when opening the script in the SPM batch as well as the provided comments and README file. The code for the workflow in addition to the code used to conduct the aging effect and asymmetry analyses can be found here https://github.com/viko18/JunaChimp.

Acknowledgements

We would like to thank Jona Fischer for the creation of the interactive Juna.Chimp web viewer adapted from nehuba (github). This study was supported by the European Union's Horizon 2020 Research and Innovation Program under Grant Agreement No. 785907 (HBP SGA2).

514 **References**

515 Alexander GE, Chen K, Aschenbrenner M, Merkley TL, Santerre-Lemmon LE, Shamy
516 JL, Skaggs WE, Buonocore MH, Rapp PR, Barnes CA. 2008. Age-related regional
517 network of magnetic resonance imaging gray matter in the rhesus macaque. J
518 Neurosci. 28:2710–2718.
519 Amunts K, Schleicher A, Bürgel U, Mohlberg H, Uylings HBM, Zilles K. 1999. Broca's
520 region revisited: Cytoarchitecture and intersubject variability. J Comp Neurol.
521 412:319–341.
522 Amunts K, Zilles K. 2015. Architectonic Mapping of the Human Brain beyond Brodmann.
523 Neuron.
524 Anderson JR, Gallup GG. 2015. Mirror self-recognition: a review and critique of
525 attempts to promote and engineer self-recognition in primates. Primates. 56:317–
526 326.
527 Ashburner J, Friston KJ. 2000. Voxel-based morphometry--the methods. Neuroimage.
528 11:805–821.
529 Ashburner J, Friston KJ. 2005. Unified segmentation. Neuroimage. 26:839–851.
530 Ashburner J, Friston KJ. 2011. Diffeomorphic registration using geodesic shooting and
531 Gauss-Newton optimisation. Neuroimage. 55:954–967.
532 Autrey MM, Reamer LA, Mareno MC, Sherwood CC, Herndon JG, Preuss T, Schapiro
533 SJ, Hopkins WD. 2014. Age-related effects in the neocortical organization of
534 chimpanzees: gray and white matter volume, cortical thickness, and gyrification.
535 Neuroimage. 101:59–67.
536 Bailey P, Bonin GV MW. 1950. The isocortex of the chimpanzee. Urbana, IL: Univ of
537 Illinois Press.
538 Bard KA, Hopkins WD. 2018. Early Socioemotional Intervention Mediates Long-Term
539 Effects of Atypical Rearing on Structural Covariation in Gray Matter in Adult
540 Chimpanzees. Psychol Sci. 29:594–603.
541 Bogart SL, Bennett AJ, Schapiro SJ, Reamer LA, Hopkins WD. 2014. Different early
542 rearing experiences have long term effects on cortical organization in captive
543 chimpanzees (Pan troglodytes). Dev Sci. 17:161–174.
544 Bogart SL, Mangin JF, Schapiro SJ, Reamer L, Bennett AJ, Pierre PJ, Hopkins WD.

545 2012. Cortical sulci asymmetries in chimpanzees and macaques: A new look at an
546 old idea. Neuroimage. 61:533–541.
547 Chen X, Errangi B, Li L, Glasser MF, Westlye LT, Fjell AM, Walhovd KB, Hu X, Herndon
548 JG, Preuss TM, Rilling JK. 2013. Brain aging in humans, chimpanzees (Pan
549 troglodytes), and rhesus macaques (Macaca mulatta): magnetic resonance imaging
550 studies of macro- and microstructural changes. Neurobiol Aging. 34:2248–2260.
551 Chiarello C, Vazquez D, Felton A, McDowell A. 2016. Structural asymmetry of the
552 human cerebral cortex: Regional and between-subject variability of surface area,
553 cortical thickness, and local gyrification. Neuropsychologia. 93:365–379.
554 Crivello F, Tzourio-Mazoyer N, Tzourio C, Mazoyer B. 2014. Longitudinal assessment of
555 global and regional rate of grey matter atrophy in 1,172 healthy older adults:
556 Modulation by sex and age. PLoS One. 9.
557 Dahl CD, Adachi I. 2013. Conceptual metaphorical mapping in chimpanzees (Pan
558 troglodytes). Elife. 2013.
559 Dahnke R, Gaser C. 2017. Voxel-based Preprocessing in CAT. Organ Hum Brain
560 Mapp.
561 Emery Thompson M, Fox SA, Berghänel A, Sabbi KH, Phillips-Garcia S, Enigk DK, Otali
562 E, Machanda ZP, Wrangham RW, Muller MN. 2020. Wild chimpanzees exhibit
563 humanlike aging of glucocorticoid regulation. Proc Natl Acad Sci. 201920593.
564 Franke K, Clarke GD, Dahnke R, Gaser C, Kuo AH, Li C, Schwab M, Nathanielsz PW.
565 2017. Premature Brain Aging in Baboons Resulting from Moderate Fetal
566 Undernutrition. Front Aging Neurosci. 9:92.
567 Freeman HD, Cantalupo C, Hopkins WD. 2004. Asymmetries in the hippocampus and
568 amygdala of chimpanzees (Pan troglodytes). Behav Neurosci. 118:1460–1465.
569 Gannon PJ, Holloway RL, Broadfield DC, Braun AR. 1998. Asymmetry of chimpanzee
570 planum temporale: Humanlike pattern of Wernicke's brain language area homolog.
571 Science (80-). 279:220–222.
572 Gaser C, Dahnke R, Kurth K, Luders E, Alzheimer's Disease Neuroimaging Initiative.
573 2020. A computational Anatomy Toolbox for the Analysis of Structural MRI Data.
574 Neuroimage. (Under review)
575 Gilissen EP, Hopkins WD. 2013. Asymmetries of the parietal operculum in chimpanzees

576 (Pan troglodytes) in relation to handedness for tool use. Cereb Cortex. 23:411–422.
577 Gomez-Robles A, Hopkins WD, Sherwood CC. 2013. Increased morphological
578 asymmetry, evolvability and plasticity in human brain evolution. Proc Biol Sci.
579 280:20130575.
580 Good CD, Johnsrude I, Ashburner J, Henson RNA, Friston KJ, Frackowiak RSJ. 2001a.
581 Cerebral asymmetry and the effects of sex and handedness on brain structure: A
582 voxel-based morphometric analysis of 465 normal adult human brains.
583 Neuroimage. 14:685–700.
584 Good CD, Johnsrude IS, Ashburner J, Henson RN, Friston KJ, Frackowiak RS. 2001b.
585 A voxel-based morphometric study of ageing in 465 normal adult human brains.
586 Neuroimage. 14:21–36.
587 Hecht EE, Mahovetz LM, Preuss TM, Hopkins WD. 2017. A neuroanatomical predictor
588 of mirror self-recognition in chimpanzees. Soc Cogn Affect Neurosci. 12:37–48.
589 Herndon JG, Tigges J, Anderson DC, Klumpp SA, McClure HM. 1999. Brain weight
590 throughout the life span of the chimpanzee. J Comp Neurol. 409:567–572.
591 Holm S. 1979. A Simple Sequentially Rejective Multiple Test Procedure. Scand J Stat.
592 6:65–70.
593 Hopkins WD, Avants BB. 2013. Regional and hemispheric variation in cortical thickness
594 in chimpanzees (Pan troglodytes). J Neurosci. 33:5241–5248.
595 Hopkins WD, Cantalupo C. 2004. Handedness in chimpanzees (Pan troglodytes) is
596 associated with asymmetries of the primary motor cortex but not with homologous
597 language areas. Behav Neurosci. 118:1176–1183.
598 Hopkins WD, Cantalupo C, Taglialatela J. 2007. Handedness Is Associated with
599 Asymmetries in Gyrification of the Cerebral Cortex of Chimpanzees. Cereb Cortex.
600 17:1750–1756.
601 Hopkins WD, Li X, Crow T, Roberts N. 2017. Vertex- and atlas-based comparisons in
602 measures of cortical thickness, gyrification and white matter volume between
603 humans and chimpanzees. Brain Struct Funct. 222:229–245.
604 Hopkins WD, Meguerditchian A, Coulon O, Bogart S, Mangin JF, Sherwood CC,
605 Grabowski MW, Bennett AJ, Pierre PJ, Fears S, Woods R, Hof PR, Vauclair J.
606 2014a. Evolution of the central sulcus morphology in primates. Brain Behav Evol.

607 84:19–30.
608 Hopkins WD, Meguerditchian A, Coulon O, Bogart S, Mangin JF, Sherwood CC,
609 Grabowski MW, Bennett AJ, Pierre PJ, Fears S, Woods R, Hof PR, Vauclair J.
610 2014b. Evolution of the Central Sulcus Morphology in Primates. Brain Behav Evol.
611 84:19–30.
612 Hopkins WD, Misiura M, Pope SM, Latash EM. 2015. Behavioral and brain asymmetries
613 in primates: A preliminary evaluation of two evolutionary hypotheses. Ann N Y Acad
614 Sci. 1359:65–83.
615 Hopkins WD, Nir TM. 2010. Planum temporale surface area and grey matter
616 asymmetries in chimpanzees (Pan troglodytes): The effect of handedness and
617 comparison with findings in humans. Behav Brain Res. 208:436–443.
618 Hopkins WD, Taglialatela JP, Meguerditchian A, Nir T, Schenker NM, Sherwood CC.
619 2008. Gray matter asymmetries in chimpanzees as revealed by voxel-based
620 morphometry. Neuroimage. 42:491–497.
621 Jagust W. 2016. Is amyloid-β harmful to the brain? Insights from human imaging
622 studies. Brain. 139:23–30.
623 Jagust W. 2018. Imaging the evolution and pathophysiology of Alzheimer disease. Nat
624 Rev Neurosci.
625 Keller SS, Roberts N, Hopkins W. 2009. A Comparative Magnetic Resonance Imaging
626 Study of the Anatomy, Variability, and Asymmetry of Broca's Area in the Human
627 and Chimpanzee Brain. J Neurosci. 29:14607–14616.
628 Kennedy KM, Erickson KI, Rodrigue KM, Voss MW, Colcombe SJ, Kramer AF, Acker
629 JD, Raz N. 2009. Age-related differences in regional brain volumes: A comparison
630 of optimized voxel-based morphometry to manual volumetry. Neurobiol Aging.
631 30:1657–1676.
632 Koelkebeck K, Miyata J, Kubota M, Kohl W, Son S, Fukuyama H, Sawamoto N,
633 Takahashi H, Murai T. 2014. The contribution of cortical thickness and surface area
634 to gray matter asymmetries in the healthy human brain. Hum Brain Mapp. 35:6011–
635 6022.
636 Kong XZ, Mathias SR, Guadalupe T, Abé C, Agartz I, Akudjedu TN, Aleman A,
637 Alhusaini S, Allen NB, Ames D, Andreassen OA, Vasquez AA, Armstrong NJ,

Bergo F, Bastin ME, Batalla A, Bauer J, Baune BT, Baur-Streubel R, Biederman J, Blaine SK, Boedhoe P, Bøen E, Bose A, Bralten J, Brandeis D, Brem S, Brodaty H, Yüksel D, Brooks SJ, Buitelaar J, Bürger C, Bülow R, Calhoun V, Calvo A, Canales-Rodríguez EJ, Canive JM, Cannon DM, Caparelli EC, Castellanos FX, Cavalleri GL, Cendes F, Chaim-Avancini TM, Chantiluke K, Chen QL, Chen X, Cheng Y, Christakou A, Clark VP, Coghill D, Connolly CG, Conzelmann A, Córdova-Palomera A, Cousijn J, Crow T, Cubillo A, Dale A, Dannlowski U, De Bruttopilo SA, De Zeeuw P, Deary IJ, Delanty N, Demeter D V., Di Martino A, Dickie EW, Dietsche B, Doan NT, Doherty CP, Doyle A, Durston S, Earl E, Ehrlich S, Ekman CJ, Elvsåshagen T, Epstein JN, Fair DA, Faraone S V., Fernández G, Filho GB, Förster K, Fouche JP, Foxe JJ, Frodl T, Fuentes-Claramonte P, Fullerton J, Garavan H, Garcia DDS, Gotlib IH, Goudriaan AE, Grabe HJ, Groenewold NA, Grotegerd D, Gruber O, Gurholt T, Haavik J, Hahn T, Hansell NK, Harris MA, Hartman CA, Hernández MDCV, Heslenfeld D, Hester R, Hibar DP, Ho BC, Ho TC, Hoekstra PJ, Van Holst RJ, Hoogman M, Høvik MF, Howells FM, Hugdahl K, Huyser C, Ingvar M, Irwin L, Ishikawa A, James A, Jahanshad N, Jernigan TL, Jönsson EG, Kähler C, Kaleda V, Kelly C, Kerich M, Keshavan MS, Khadka S, Kircher T, Kohls G, Konrad K, Korucuoglu O, Krämer B, Krug A, Kwon JS, Lambregts-Rommelse N, Landén M, Lázaro L, Lebedeva I, Lenroot R, Lesch KP, Li Q, Lim KO, Liu J, Lochner C, London ED, Lonning V, Lorenzetti V, Luciano M, Luijten M, Lundervold AJ, MacKey S, MacMaster FP, Maingault S, Malpas CB, Malt UF, Mataix-Cols D, Martin-Santos R, Mayer AR, McCarthy H, Mitchell PB, Mueller BA, Maniega SM, Mazoyer B, McDonald C, McLellan Q, McMahon KL, McPhilemy G, Momenan R, Morales AM, Narayanaswamy JC, Moreira JCV, Nerland S, Nestor L, Newman E, Nigg JT, Nordvik JE, Novotny S, Weiss EO, O'Gorman RL, Oosterlaan J, Oranje B, Orr C, Overs B, Pauli P, Paulus M, Plessen KJ, Von Polier GG, Pomarol-Clotet E, Portella MJ, Qiu J, Radua J, Ramos-Quiroga JA, Reddy YCJ, Reif A, Roberts G, Rosa P, Rubia K, Sacchet MD, Sachdev PS, Salvador R, Schmaal L, Schulte-Rüther M, Schweren L, Seidman L, Seitz J, Serpa MH, Shaw P, Shumskaya E, Silk TJ, Simmons AN, Simulionyte E, Sinha R, Sjoerds Z, Smelror RE, Soliva JC, Solowij N, Souza-Duran FL, Sponheim SR, Stein DJ, Stein

669 EA, Stevens M, Strike LT, Sudre G, Sui J, Tamm L, Temmingh HS, Thoma RJ,
670 Tomyshev A, Tronchin G, Turner J, Uhlmann A, Van Erp TGM, Van Den Heuvel
671 OA, Van Der Meer D, Van Eijk L, Vance A, Veer IM, Veltman DJ,
672 Venkatasubramanian G, Vilarroya O, Vives-Gilabert Y, Voineskos AN, Völzke H,
673 Vuletic D, Walitza S, Walter H, Walton E, Wardlaw JM, Wen W, Westlye LT,
674 Whelan CD, White T, Wiers RW, Wright MJ, Wittfeld K, Yang TT, Yasuda CL,
675 Yoncheva Y, Yücel M, Yun JY, Zanetti MV, Zhen Z, Zhu XX, Ziegler GC, Zierhut K,
676 De Zubicaray GI, Zwiers M, Glahn DC, Franke B, Crivello F, Tzourio-Mazoyer N,
677 Fisher SE, Thompson PM, Francks C, Farde L, Flyckt L, Engberg G, Erhardt S,
678 Fatouros-Bergman H, Cervenka S, Schwieler L, Piehl F, Collste K, Victorsson P,
679 Malmqvist A, Hedberg M, Orhan F. 2018. Mapping cortical brain asymmetry in
680 17,141 healthy individuals worldwide via the ENIGMA consortium. Proc Natl Acad
681 Sci U S A. 115:E5154–E5163.
682 Kurth F, Gaser C, Luders E. 2015. A 12-step user guide for analyzing voxel-wise gray
683 matter asymmetries in statistical parametric mapping (SPM). Nat Protoc. 10:293–
684 304.
685 La Joie R, Perrotin A, Barre L, Hommet C, Mezenge F, Ibazizene M, Camus V, Abbas
686 A, Landeau B, Guilloteau D, de La Sayette V, Eustache F, Desgranges B, Chetelat
687 G. 2012. Region-specific hierarchy between atrophy, hypometabolism, and beta-
688 amyloid (Abeta) load in Alzheimer's disease dementia. J Neurosci. 32:16265–
689 16273.
690 Langergraber KE, Prüfer K, Rowney C, Boesch C, Crockford C, Fawcett K, Inoue E,
691 Inoue-Muruyama M, Mitani JC, Muller MN, Robbins MM, Schubert G, Stoinski TS,
692 Viola B, Watts D, Wittig RM, Wrangham RW, Zuberbühler K, Pääbo S, Vigilant L.
693 2012. Generation times in wild chimpanzees and gorillas suggest earlier
694 divergence times in great ape and human evolution. Proc Natl Acad Sci U S A.
695 109:15716–15721.
696 Li X, Crow TJ, Hopkins WD, Gong Q, Roberts N. 2018. Human torque is not present in
697 chimpanzee brain. Neuroimage. 165:285–293.
698 Llado A, Tort-Merino A, Sanchez-Valle R, Falgas N, Balasa M, Bosch B, Castellvi M,
699 Olives J, Antonell A, Hornberger M. 2018. The hippocampal longitudinal axis-

700 relevance for underlying tau and TDP-43 pathology. Neurobiol Aging. 70:1–9.
701 Luders E, Narr KL, Thompson PM, Rex DE, Jancke L, Toga AW. 2006. Hemispheric
702 asymmetries in cortical thickness. Cereb Cortex. 16:1232–1238.
703 Lyn H, Pierre P, Bennett AJ, Fears S, Woods R, Hopkins WD. 2011. Planum temporale
704 grey matter asymmetries in chimpanzees (Pan troglodytes), vervet (Chlorocebus
705 aethiops sabaeus), rhesus (Macaca mulatta) and bonnet (Macaca radiata)
706 monkeys. Neuropsychologia. 49:2004–2012.
707 Mai JK, Majtanik M, Paxinos G. 2015. Atlas of the Human Brain. Elsevier Science.
708 Maingault S, Tzourio-Mazoyer N, Mazoyer B, Crivello F. 2016. Regional correlations
709 between cortical thickness and surface area asymmetries: A surface-based
710 morphometry study of 250 adults. Neuropsychologia. 93:350–364.
711 Marie D, Roth M, Lacoste R, Nazarian B, Bertello A, Anton JL, Hopkins WD,
712 Margiotoudi K, Love SA, Meguerditchian A. 2018. Left Brain Asymmetry of the
713 Planum Temporale in a Nonhominid Primate: Redefining the Origin of Brain
714 Specialization for Language. Cereb Cortex. 28:1808–1815.
715 Mazziotta J, Toga A, Evans A, Fox P, Lancaster J, Zilles K, Woods R, Paus T, Simpson
716 G, Pike B, Holmes C, Collins L, Thompson P, MacDonald D, Iacoboni M,
717 Schormann T, Amunts K, Palomero-Gallagher N, Geyer S, Parsons L, Narr K,
718 Kabani N, Le Goualher G, Boomsma D, Cannon T, Kawashima R, Mazoyer B.
719 2001. A probabilistic atlas and reference system for the human brain: International
720 Consortium for Brain Mapping (ICBM). Philos Trans R Soc B Biol Sci.
721 Minkova L, Habich A, Peter J, Kaller CP, Eickhoff SB, Klöppel S. 2017. Gray matter
722 asymmetries in aging and neurodegeneration: A review and meta-analysis. Hum
723 Brain Mapp. 38:5890–5904.
724 Plessen KJ, Hugdahl K, Bansal R, Hao X, Peterson BS. 2014. Sex, age, and cognitive
725 correlates of asymmetries in thickness of the cortical mantle across the life span. J
726 Neurosci. 34:6294–6302.
727 Rajapakse JC, Giedd JN, Rapoport JL. 1997. Statistical approach to segmentation of
728 single-channel cerebral mr images. IEEE Trans Med Imaging. 16:176–186.
729 Rilling JK, Insel TR. 1999. The primate neocortex in comparative perspective using
730 magnetic resonance imaging. J Hum Evol. 37:191–223.

731 Savage-Rumbaugh ES. 1986. Ape language : from conditioned response to symbol.
732 Oxford University Press.
733 Savage-Rumbaugh ES, Lewin R. 1994. Kanzi : the ape at the brink of the human mind.
734 Wiley.
735 Schenker NM, Hopkins WD, Spocter MA, Garrison AR, Stimpson CD, Erwin JM, Hof
736 PR, Sherwood CC. 2010. Broca's Area Homologue in Chimpanzees (Pan
737 troglodytes): Probabilistic Mapping, Asymmetry, and Comparison to Humans.
738 Cereb Cortex. 20:730–742.
739 Shamy JL, Habeck C, Hof PR, Amaral DG, Fong SG, Buonocore MH, Stern Y, Barnes
740 CA, Rapp PR. 2011. Volumetric correlates of spatiotemporal working and
741 recognition memory impairment in aged rhesus monkeys. Cereb Cortex. 21:1559–
742 1573.
743 Sherwood CC, Broadfield DC, Holloway RL, Gannon PJ, Hof PR. 2003. Variability of
744 Broca's area homologue in African great apes: Implications for language evolution.
745 Anat Rec - Part A Discov Mol Cell Evol Biol. 271:276–285.
746 Sherwood CC, Gordon AD, Allen JS, Phillips KA, Erwin JM, Hof PR, Hopkins WD. 2011.
747 Aging of the cerebral cortex differs between humans and chimpanzees. Proc Natl
748 Acad Sci U S A. 108:13029–13034.
749 Shumaker RW, Walkup KR, Beck BB. 2011. Animal tool behavior : the use and
750 manufacture of tools by animals. Johns Hopkins University Press.
751 Smith SM, Nichols TE. 2009. Threshold-free cluster enhancement: Addressing
752 problems of smoothing, threshold dependence and localisation in cluster inference.
753 Neuroimage. 44:83–98.
754 Spocter MA, Hopkins WD, Garrison AR, Bauernfeind AL, Stimpson CD, Hof PR,
755 Sherwood CC. 2010. Wernicke's area homologue in chimpanzees IPan troglodytes
756 and its relation to the appearance of modern human language. Proc R Soc B Biol
757 Sci. 277:2165–2174.
758 Taglialatela JP, Cantalupo C, Hopkins WD. 2006. Gesture handedness predicts
759 asymmetry in the chimpanzee inferior frontal gyrus. Neuroreport. 17:923–927.
760 Toga AW, Thompson PM. 2003. Mapping brain asymmetry. Nat Rev Neurosci. 4:37–48.
761 Tohka J, Zijdenbos A, Evans A. 2004. Fast and robust parameter estimation for

762 statistical partial volume models in brain MRI. Neuroimage. 23:84–97.
763 Tomasello M, Call J. 1997. Primate Cognition.
764 Uylings HBM, Jacobsen AM, Zilles K, Amunts K. 2006. Left-right asymmetry in volume
765 and number of neurons in adult Broca's area. Cortex. 42:652–658.
766 Waal FBM de (Frans BM. 1996. Good natured : the origins of right and wrong in humans
767 and other animals. Harvard University Press.
768 Waterson RH, Lander ES, Wilson RK. 2005. Initial sequence of the chimpanzee
769 genome and comparison with the human genome. Nature. 437:69–87.
770 Watkins KE. 2001. Structural Asymmetries in the Human Brain: a Voxel-based
771 Statistical Analysis of 142 MRI Scans. Cereb Cortex. 11:868–877.
772 Xiang L, Crow T, Roberts N. 2019. Cerebral torque is human specific and unrelated to
773 brain size. Brain Struct Funct. 224:1141–1150.
774 Zhou D, Lebel C, Evans A, Beaulieu C. 2013. Cortical thickness asymmetry from
775 childhood to older adulthood. Neuroimage. 83:66–74.
776 Zilles K, Armstrong E, Moser KH, Schleicher A, Stephan H. 1989. Gyrification in the
777 cerebral cortex of primates. Brain Behav Evol. 34:143–150.
778 Zilles K, Dabringhaus A, Geyer S, Amunts K, Qü M, Schleicher A, Gilissen E, Schlaug
779 G, Steinmetz H. 1996. Structural asymmetries in the human forebrain and the
780 forebrain of non- human primates and rats. In: Neuroscience and Biobehavioral
781 Reviews. Elsevier Ltd. p. 593–605.
782

783 **Supplementary**

784 Supplementary 1.1 DICOM conversion and De-noising

785 The structural T1-weighted images were provided by the NCBR in their original
786 DICOM format and converted into Nifti using MRIcron (Rorder and Brett 2000). If multi-
787 ple scans were available, the average was computed. Following DICOM conversion
788 each image was cleaned of noise (Manjon et al. 2010) and signal inhomogeneity and
789 resliced to 0.6 mm isotropic resolution. Finally, the anterior commissure was manually
790 set as the center (0,0,0) of all Nifti's to aid in affine preprocessing.
791

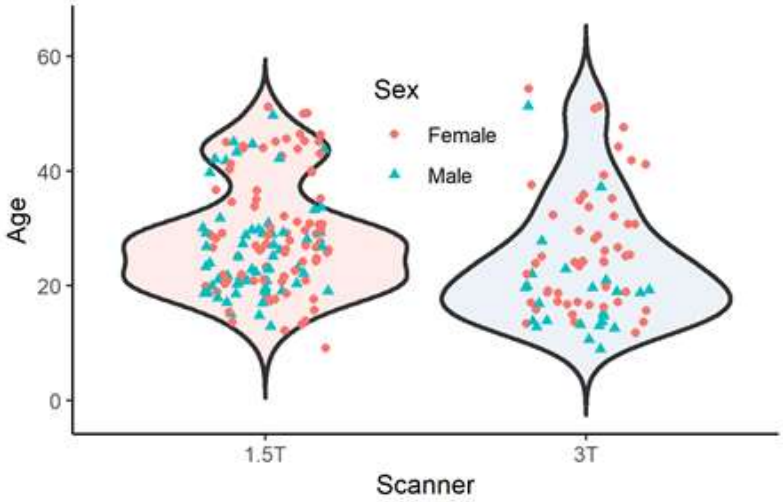

Supplementary Figure 1. Age and sex distribution of complete 223 chimpanzees separated by scanner strength.

Supplementary 1.2 Chimpanzee QC

CAT12 provides quality measures pertaining to noise, bias inhomogeneities, resolution and an overall compounded score of the original input image. Using these ratings, poor images were flagged for visual inspection when they were 2 standard deviations (std) away from the sample mean of each rating. The preprocessed modulated GM maps were then tested for sample inhomogeneity separately for each scanner (3T & 1.5T) and those that have a mean correlation below 2 std were flagged for visual inspection. Once the original image was flagged, affine GM, and modulated GM maps were inspected for poor quality, tissue misclassification, artefacts, irregular deformations, and very high intensities. For the second iteration, the passed modulated GM maps were tested again for mean correlation as a complete sample, flagging the images below 3 std for visual inspection. Looking for the same features as in the initial QC iteration. Following the two iterations of QC a total of 178 of 223 chimpanzee MRI's (120 females, 11 – 54 y/o, mean = 26.7 ± 9.8) qualified for statistical analysis.

Supplementary 1.3 CAT12 Preprocessing Segmentation

Structural image segmentation in CAT12 builds on the TPM-based approach employed by SPM12, whereby, the gray/white image intensity is aided with a priori tissue

probabilities in initial segmentation and affine registration as it is in common template space. Another advantage of a TPM is that one has a template for initial affine registration, which then enables the segment maps to be non-linearly registered and spatially normalized to corresponding segment maps of the chimpanzee shooting templates. Lowering the possibility for registration errors improves the quality of the final normalized image. Improving upon SPM's segmentation (Ashburner and Friston 2005), CAT12 employs Local Adaptive Segmentation (LAS) (Dahnke et al. 2012), Adaptive Maximum A Posterior segmentation(AMAP) (Dahnke and Gaser 2017; Gaser et al. 2020), and Partial Volume Estimation (PVE) (Tohka et al. 2004). LAS creates local intensity transformations for all tissue types to limit GM misclassification due to varying GM intensity in regions such as the occipital, basal ganglia, and motor cortex as a result of anatomical properties (e.g. high myelination and iron content). AMAP segmentation takes the initially segmented, aligned, and skull stripped image created utilizing the TPM and disregards the a priori information of the TPM, to conduct an adaptive AMAP estimation where local variations are modelled by slowly varying spatial functions (Rajapakse et al. 1997). Along with the classical three tissue types for segmentation (GM, WM, & CSF) based on the AMAP estimation, an additional two PVE classes (GM-WM & GM-CSF) are created resulting in an estimate of the fraction of each tissue type contained in each voxel. These features outlined above of our pipeline allow for more accurate tissue segmentation and therefore a better representation of macroanatomical GM levels for analysis.

Supplementary Table 1. Davi130 Labels

Label Number	Davi130 Label	Brain Region	Hemisphere	Acronyms
1	Anterior Superior Frontal Gyrus	Frontal	left	L.aSFG
2	Anterior Superior Frontal Gyrus	Frontal	right	R.aSFG
3	Middle Superior Frontal Gyrus	Frontal	left	L.mSFG
4	Middle Superior Frontal Gyrus	Frontal	right	R.mSFG
5	Posterior Superior Frontal Gyrus	Frontal	left	L.Hth
6	Posterior Superior Frontal Gyrus	Frontal	right	R.pSFG
7	Anterior Middle Frontal Gyrus	Frontal	left	L.aMFG
8	Anterior Middle Frontal Gyrus	Frontal	right	R.aMFG
9	Posterior Middle Frontal Gyrus	Frontal	left	L.pMFG
10	Posterior Middle Frontal Gyrus	Frontal	right	R.pMFG

11	Anterior Inferior Frontal Gyrus	Frontal	left	L.aIFG
12	Anterior Inferior Frontal Gyrus	Frontal	right	R.aIFG
13	Middle Inferior Frontal Gyrus	Frontal	left	L.mIFG
14	Middle Inferior Frontal Gyrus	Frontal	right	R.mIFG
15	Posterior Inferior Frontal Gyrus	Frontal	left	L.pIFG
16	Posterior Inferior Frontal Gyrus	Frontal	right	R.pIFG
17	Medial Orbitofrontal Cortex	Frontal	left	L.mOFC
18	Medial Orbitofrontal Cortex	Frontal	right	R.mOFC
19	Lateral Orbitofrontal Cortex	Frontal	left	L.lOFC
20	Lateral Orbitofrontal Cortex	Frontal	right	R.lOFC
21	Anterior Cingulate Cortex	Limbic	left	L.ACC
22	Anterior Cingulate Cortex	Limbic	right	R.ACC
23	Middle Cingulate Cortex	Limbic	left	L.MCC
24	Middle Cingulate Cortex	Limbic	right	R.MCC
25	Posterior Cingulate Cortex	Limbic	left	L.PCC
26	Posterior Cingulate Cortex	Limbic	right	R.PCC
27	Superior Precentral Gyrus	Frontal	left	L.sPrCG
28	Superior Precentral Gyrus	Frontal	right	R.sPrCG
29	Middle Precentral Gyrus	Frontal	left	L.mPrCG
30	Middle Precentral Gyrus	Frontal	right	R.mPrCG
31	Inferior Precentral Gyrus	Frontal	left	L.iPrCG
32	Inferior Precentral Gyrus	Frontal	right	R.iPrCG
33	Paracentral Lobule	Parietal	left	L.PCL
34	Paracentral Lobule	Parietal	right	R.PCL
35	Frontal Operculum	Frontal	left	L.FOP
36	Frontal Operculum	Frontal	right	R.FOP
37	Parietal Operculum	Parietal	left	L.POP
38	Parietal Operculum	Parietal	right	R.POP
39	Anterior Insula	Temporal	left	L.aIns
40	Anterior Insula	Temporal	right	R.aIns
41	Posterior Insula	Temporal	left	L.pIns
42	Posterior Insula	Temporal	right	R.pIns
43	Anterior Transverse Temporal Gyrus	Temporal	left	L.aTTG
44	Anterior Transverse Temporal Gyrus	Temporal	right	R.aTTG
45	Posterior Transverse Temporal Gyrus	Temporal	left	L.pTTG
46	Posterior Transverse Temporal Gyrus	Temporal	right	R.pTTG
47	Anterior Superior Temporal Gyrus	Temporal	left	L.aSTG
48	Anterior Superior Temporal Gyrus	Temporal	right	R.aSTG
49	Posterior Superior Temporal Gyrus	Temporal	left	L.pSTG
50	Posterior Superior Temporal Gyrus	Temporal	right	R.pSTG
51	Anterior Middle Temporal Gyrus	Temporal	left	L.aMTG
52	Anterior Middle Temporal Gyrus	Temporal	right	R.aMTG
53	Posterior Middle Temporal Gyrus	Temporal	left	L.pMTG

54	Posterior Middle Temporal Gyrus	Temporal	right	R.pMTG
55	Anterior Inferior Temporal Gyrus	Temporal	left	L.aITG
56	Anterior Inferior Temporal Gyrus	Temporal	right	R.aITG
57	Posterior Inferior Temporal Gyrus	Temporal	left	L.pITG
58	Posterior Inferior Temporal Gyrus	Temporal	right	R.pITG
59	Entorhinal Cortex	Limbic	left	L.EHC
60	Entorhinal Cortex	Limbic	right	R.EHC
61	Anterior Fusiform Gyrus	Temporal	left	L.aFFG
62	Anterior Fusiform Gyrus	Temporal	right	R.aFFG
63	Posterior Fusiform Gyrus	Temporal	left	L.pFFG
64	Posterior Fusiform Gyrus	Temporal	right	R.pFFG
65	Parahippocampal Gyrus	Limbic	left	L.PHC
66	Parahippocampal Gyrus	Limbic	right	R.PHC
67	Amygdala	Limbic	left	L.Amy
68	Amygdala	Limbic	right	R.Amy
69	Hippocampus	Limbic	left	L.HC
70	Hippocampus	Limbic	right	R.HC
71	Superior Postcentral Gyrus	Parietal	left	L.sPoCG
72	Superior Postcentral Gyrus	Parietal	right	R.sPoCG
73	Middle Postcentral Gyrus	Parietal	left	L.mPoCG
74	Middle Postcentral Gyrus	Parietal	right	R.mPoCG
75	Inferior Postcentral Gyrus	Parietal	left	L.iPoCG
76	Inferior Postcentral Gyrus	Parietal	right	R.iPoCG
77	Superior Parietal Lobule	Parietal	left	L.SPL
78	Superior Parietal Lobule	Parietal	right	R.SPL
79	Supramarginal Gyrus	Parietal	left	L.SMG
80	Supramarginal Gyrus	Parietal	right	R.SMG
81	Angular Gyrus	Parietal	left	L.AnG
82	Angular Gyrus	Parietal	right	R.AnG
83	Precuneus	Parietal	left	L.PCun
84	Precuneus	Parietal	right	R.PCun
85	Cuneus	Occipital	left	L.Cun
86	Cuneus	Occipital	right	R.Cun
87	Lingual Gyrus	Occipital	left	L.LG
88	Lingual Gyrus	Occipital	right	R.LG
89	Calcarine Sulcus	Occipital	left	L.Calc
90	Calcarine Sulcus	Occipital	right	R.Calc
91	Superior Occipital Gyrus	Occipital	left	L.sOG
92	Superior Occipital Gyrus	Occipital	right	R.sOG
93	Middle Occipital Gyrus	Occipital	left	L.mOG
94	Middle Occipital Gyrus	Occipital	right	R.mOG
95	Inferior Occipital Gyrus	Occipital	left	L.iOG
96	Inferior Occipital Gyrus	Occipital	right	R.iOG

97	Caudate Nucleus	Basal Ganglia	left	L.CN
98	Caudate Nucleus	Basal Ganglia	right	R.CN
99	Nucleus Accumbens	Basal Ganglia	left	L.NA
100	Nucleus Accumbens	Basal Ganglia	right	R.NA
101	Basal Forebrain Nuclei	Basal Ganglia	left	L.BF
102	Basal Forebrain Nuclei	Basal Ganglia	right	R.BF
103	Putamen	Basal Ganglia	left	L.Pu
104	Putamen	Basal Ganglia	right	R.Pu
105	Globus pallidus	Basal Ganglia	left	L.GP
106	Globus pallidus	Basal Ganglia	right	R.GP
107	Thalamus	Basal Ganglia	left	L.Th
108	Thalamus	Basal Ganglia	right	R.Th
109	Hypothalamus	Basal Ganglia	left	L.HTh
110	Hypothalamus	Basal Ganglia	right	R.HTh
111	Cerebellum IX-Tonsil	Cerebellum	left	L.CerIX
112	Cerebellum IX-Tonsil	Cerebellum	right	R.CerIX
113	Cerebellum VIIIAB-Inferior Posterior - PML	Cerebellum	left	L.CerVIII
114	Cerebellum VIIIAB-Inferior Posterior - PML	Cerebellum	right	R.CerVIII
115	Cerebellum VIIA - Superior Posterior - Crus I of Ansiform Lobule	Cerebellum	left	L.CrusI
116	Cerebellum VIIA - Superior Posterior – Crus I of Ansiform Lobule	Cerebellum	right	R.CrusI
117	Cerebellum VIIA - Superior Posterior – Crus II of Ansiform Lobule with Par-amedian 1	Cerebellum	left	L.CrusII
118	Cerebellum VIIA-Superior Posterior - Crus II of Ansiform Lobule with Para-median 1	Cerebellum	right	R.CrusII
119	Cerebellum VI-Superior Posterior	Cerebellum	left	L.CerVI
120	Cerebellum VI-Superior Posterior	Cerebellum	right	R.CerVI
121	Cerebellum V-Anterior B	Cerebellum	left	L.CerVB
122	Cerebellum V-Anterior B	Cerebellum	right	R.CerVB
123	Cerebellum V-Anterior A	Cerebellum	left	L.CerVA
124	Cerebellum V-Anterior A	Cerebellum	right	R.CerVA
125	Cerebellum IV-Anterior Quadrangu-late	Cerebellum	left	L.CerIV
126	Cerebellum IV-Anterior Quadrangu-late	Cerebellum	right	R.CerIV
127	Cerebellum III-Anterior Quadrangulate	Cerebellum	left	L.CerIII
128	Cerebellum III-Anterior Quadrangulate	Cerebellum	right	R.CerIII
129	Cerebellum II-Anterior Quadrangulate	Cerebellum	left	L.CerII
130	Cerebellum II-Anterior Quadrangulate	Cerebellum	right	R.CerII

837 Supplementary Table 2. DaVi Labels Age Effect on Gray Matter Volume

Davi130 Label	*T-statistic*	*p-value*
Frontal Cortex		
Anterior Superior Frontal Gyrus (L.aSFG)	-1.57	0.1197
Anterior Superior Frontal Gyrus (R.aSFG)	-1.16	0.2482
Middle Superior Frontal Gyrus (L.mSFG)*	-3.59	0.0004
Middle Superior Frontal Gyrus (R.mSFG)	-3.55	0.0005
Posterior Superior Frontal Gyrus (L.pSFG)	-3.18	0.0017
Posterior Superior Frontal Gyrus (R.pSFG)	-2.35	0.0199
Anterior Middle Frontal Gyrus (L.aMFG)	-1.08	0.2814
Anterior Middle Frontal Gyrus (R.aMFG)	-2.11	0.0365
Posterior Middle Frontal Gyrus (L.pMFG)	-1.88	0.0614
Posterior Middle Frontal Gyrus (R.pMFG)	-1.79	0.0757
Anterior Inferior Frontal Gyrus (L.aIFG)	-1.27	0.2048
Anterior Inferior Frontal Gyrus (R.aIFG)	-1.52	0.1300
Middle Inferior Frontal Gyrus (L.mIFG)	-1.79	0.0747
Middle Inferior Frontal Gyrus (R.mIFG)	-2.65	0.0089
Posterior Inferior Frontal Gyrus (L.pIFG)	-2.83	0.0052
Posterior Inferior Frontal Gyrus (R.pIFG)	-2.00	0.0468
Medial Orbitofrontal Cortex (L.mOFC)	-1.82	0.0711
Medial Orbitofrontal Cortex (R.mOFC)	-1.83	0.0697
Lateral Orbitofrontal Cortex (L.lOFC)*	-4.31	3.0×10^{-5}
Lateral Orbitofrontal Cortex (R.lOFC)*	-3.79	0.0002
Superior Precentral Gyrus (L.sPrCG)	-1.96	0.0511
Superior Precentral Gyrus (R.sPrCG)	-0.47	0.6380
Middle Precentral Gyrus (L.mPrCG)	-1.96	0.0519
Middle Precentral Gyrus (R.mPrCG)	-1.34	0.1836
Inferior Precentral Gyrus (L.iPrCG)	-1.78	0.0766
Inferior Precentral Gyrus (R.iPrCG)	-1.20	0.2312
Frontal Operculum (L.FOP)	-2.74	0.0067
Frontal Operculum (R.FOP)	-1.55	0.1227
Limbic Cortex		
Anterior Cingulate Gyrus (L.ACC)	-2.66	0.0085
Anterior Cingulate Gyrus (R.ACC)	-3.08	0.0024
Middle Cingulate Gyrus (L.MCC)*	-4.02	8.78×10^{-5}
Middle Cingulate Gyrus (R.MCC)*	-4.29	2.99×10^{-5}
Posterior Cingulate Gyrus (L.PCC)	-3.37	0.0009
Posterior Cingulate Gyrus (R.PCC)*	-3.81	0.0002
Entorhinal Cortex (L.EG)	-0.43	0.6685
Entorhinal Cortex (R.EG)	-1.22	0.2229
Parahippocampal Gyrus (L.PHC)	-2.70	0.0077
Parahippocampal Gyrus (R.PHC)	-3.15	0.0019
Amygdala (L.Amy)	-3.26	0.0014

Amygdala (R.Amy)	-2.73	0.0070
Hippocampus (L.HC)	-0.72	0.4735
Hippocampus (R.HC)	-1.19	0.2366
Temporal Cortex		
Anterior Insula (L.aIns)	-2.92	0.0040
Anterior Insula (R.aIns)	-3.09	0.0024
Posterior Insula (L.pIns)	-1.87	0.0631
Posterior Insula (R.pIns)	-2.01	0.0463
Anterior Transverse Temporal Gyrus (L.aTTG*	-4.77	3.90×10^{-6}
Anterior Transverse Temporal Gyrus (R.aTTG)	-3.15	0.0019
Posterior Transverse Temporal Gyrus (R.pTTG)	-2.35	0.0198
Posterior Transverse Temporal Gyrus (L.pTTG)	-2.52	0.0126
Anterior Superior Temporal Gyrus (L.aSTG)	-2.57	0.0111
Anterior Superior Temporal Gyrus (R.aSTG)	-1.53	0.1269
Posterior Superior Temporal Gyrus (L.pSTG)	-2.60	0.0103
Posterior Superior Temporal Gyrus (R.pSTG)	-3.26	0.0014
Anterior Middle Temporal Gyrus (L.aMTG)	-1.74	0.0837
Anterior Middle Temporal Gyrus (R.aMTG)	-1.36	0.1759
Posterior Middle Temporal Gyrus (L.pMTG)	-1.06	0.2888
Posterior Middle Temporal Gyrus (R.pMTG)	-0.95	0.3456
Anterior Inferior Temporal Gyrus (L.aITG)	-2.15	0.0327
Anterior Inferior Temporal Gyrus (R.aITG)	-2.35	0.0201
Posterior Inferior Temporal Gyrus (L.pITG)	-1.83	0.0689
Posterior Inferior Temporal Gyrus (R.pITG)	-2.92	0.0040
Anterior Fusiform Gyrus (L.aFFG)	-2.12	0.0354
Anterior Fusiform Gyrus (R.aFFG)	-2.20	0.0291
Posterior Fusiform Gyrus (L.pFFG)	-3.47	0.0007
Posterior Fusiform Gyrus (R.pFFG)	-3.49	0.0006
Parietal Cortex		
Superior Postcentral Gyrus (L.sPotCG)	-2.25	0.0260
Superior Postcentral Gyrus (R.sPoCG)	-0.50	0.6196
Middle Postcentral Gyrus (L.mPoCG)	-1.18	0.2409
Middle Postcentral Gyrus (R.mPoCG)	-0.41	0.6851
Inferior Postcentral Gyrus (L.iPoCG)	-1.96	0.0516
Inferior Postcentral Gyrus (R.iPoCG)	-0.66	0.5092
Superior Parietal Lobule (L.SPL)	-2.06	0.0412
Superior Parietal Lobule (R.SPL)	-1.25	0.2121
Supramarginal Gyrus (L.SMG)	-1.38	0.1688
Supramarginal Gyrus (R.SMG)	-1.22	0.2222
Angular Gyrus (L.AG)	-2.25	0.0257
Angular Gyrus (R.AG)	-1.68	0.0942
Parietal Operculum (L.POP)	-1.82	0.0699
Parietal Operculum (R.POP)	-0.82	0.4149

Paracentral Lobule (L.PCL)	-1.51	0.1321
Paracentral Lobule (R.PCL)	-0.63	0.5305
Precuneus (L.PCun)	-3.48	0.0006
Precuneus (R.PCun)*	-3.93	0.0001
Occipital		
Cuneus (L.Cun)	-1.99	0.0485
Cuneus (R.Cun)	-2.66	0.0085
Lingual Gyrus (L.LG)	-3.30	0.0012
Lingual Gyrus (R.LG)*	-4.11	0.0001
Calcarine Sulcus (R.Calc)	-3.04	0.0028
Calcarine Sulcus (L.Calc)*	-3.75	0.0002
Superior Occipital Gyrus (L.sOG)	-1.85	0.0657
Superior Occipital Gyrus (R.sOG)	-2.23	0.0267
Middle Occipital Gyrus (L.mOG)	0.34	0.7351
Middle Occipital Gyrus (R.mOG)	-0.75	0.4525
Inferior Occipital Gyrus (L.iOG)	-0.53	0.5947
Inferior Occipital Gyrus (R.iOG)	-1.19	0.2345
Basal Ganglia		
Caudate Nuclues (L.CN)*	-5.05	1.12×10^{-6}
Caudate Nuclues (R.CN)*	-5.70	4.99×10^{-8}
Nucleus Accumbens (L.NA)*	-4.77	3.84×10^{-6}
Nucleus Accumbens (R.NA)*	-4.23	3.81×10^{-5}
Basal Forebrain Nuclei (L.BF)	-1.25	0.2131
Basal Forebrain Nuclei (R.BF)	-1.77	0.0792
Putamen (L.Pu)*	-6.18	4.55×10^{-9}
Putamen (R.Pu)*	-6.68	3.10×10^{-10}
Globus Pallidus (L.GP)	1.68	0.0954
Globus Pallidus (R.GP)	2.72	0.0073
Thalamus (L.Tha)	-0.40	0.6920
Thalamus (R.Tha)	1.12	0.2653
Hypothalamus (L.HTh)	-1.78	0.0762
Hypothalamus (R.HTh)	-1.42	0.1570
Cerebellum		
Cerebellum IX-Tonsil (L.CerIX)	-2.46	0.0149
Cerebellum IX-Tonsil (R.CerIX)	-2.83	0.0052
Cerebellum VIIIAB-Inferior Posterior -PML (L.CerVIIIAB)	-2.46	0.0147
Cerebellum VIIIAB-Inferior Posterior -PML (R.CerVIIIAB)	-3.00	0.0031
Cerebellum VIIA-Superior Posterior -Crus I (L.CrusI)	-1.29	0.1971
Cerebellum VIIA-Superior Posterior -Crus I (R.CrusI)	-1.94	0.0543
Cerebellum VIIA-Superior Posterior -Crus II (L.CrusII)	-2.79	0.0059
Cerebellum VIIA-Superior Posterior -Crus II (R.CrusII)*	-3.75	0.0002
Cerebellum VI-Superior Posterior (L.CerVI)	-3.17	0.0018

Cerebellum VI-Superior Posterior (R.CerVI)	-3.38	0.0009
Cerebellum V-Anterior B (L.CerVB)	-2.99	0.0032
Cerebellum V-Anterior B (R.CerVB)	-3.13	0.0020
Cerebellum V-Anterior A (L.CerVA)*	-3.78	0.0002
Cerebellum V-Anterior A (R.CerVA)*	-4.91	2.09×10^{-6}
Cerebellum IV-Anterior Quadrangulate (L.CerIV)*	-4.39	1.95×10^{-5}
Cerebellum IV-Anterior Quadrangulate (R.CerIV)*	-5.75	4.02×10^{-8}
Cerebellum III-Anterior Quadrangulate (L.CerIII)*	-3.77	0.0002
Cerebellum III-Anterior Quadrangulate (R.CerIII)*	-4.42	1.75×10^{-5}
Cerebellum II-Anterior Quadrangulate (L.CerII)	-3.18	0.0018
Cerebellum II-Anterior Quadrangulate (R.CerII)	-2.83	0.0052

Key: L. refers to region in the left hemisphere, while R. the right hemisphere. * multiple comparisons correction at FWE $p \leq 0.05$.

Supplementary Table 3. Davi130 labels cortical hemispheric asymmetry

Davi130 Label	***T-statistic***	***p-value***
Leftward Asymmetry		
Frontal Cortex		
Anterior Superior Frontal Gyrus (aSFG)*	6.34	1.80×10^{-9}
Middle Superior Frontal Gyrus (mSFG)	3.14	0.0020
Anterior Middle Frontal Gyrus (aMFG)	2.07	0.0395
Posterior Middle Frontal Gyrus (pMFG)	0.84	0.4019
Anterior Inferior Frontal Gyrus (aIFG)	0.61	0.5434
Posterior Inferior Frontal Gyrus (pIFG)	2.91	0.0041
Medial Orbitofrontal Cortex (mOFC)*	4.42	1.70×10^{-5}
Superior Precentral Gyrus (sPrCG)	1.30	0.1968
Middle Precentral Gyrus (mPrCG)	2.94	0.0037
Inferior Precentral Gyrus (iPrCG)	0.15	0.8807
Limbic Cortex		
Anterior Cingulate Gyrus (ACC)	1.97	0.0502
Hippocampus (HC)*	6.70	2.70×10^{-10}
Temporal Cortex		
Anterior Insula (aIns)*	6.47	9.38×10^{-10}
Posterior Insula (pIns)*	7.63	1.38×10^{-12}
Anterior Transverse Temporal Gyrus (aTTG)	2.49	0.0138
Posterior Transverse Temporal Gyrus (pTTG)*	10.14	2.50×10^{-19}
Posterior Middle Temporal Gyrus (pMTG)	1.65	0.1011
Anterior Inferior Temporal Gyrus (aITG)	2.34	0.0202
Posterior Inferior Temporal Gyrus (pITG)	0.64	0.5206
Anterior Fusiform Gyrus (aFFG)	1.48	0.1404

Parietal Cortex		
Inferior Precentral Gyrus (iPoCG)*	6.93	7.63×10^{-11}
Supramarginal Gyrus (SMG)*	5.73	4.31×10^{-8}
Occipital Cortex		
Superior Occipital Gyrus (sOG)*	4.16	4.98×10^{-5}
Middle Occipital Gyrus (mOG)	1.22	0.2255
Inferior Occipital Gyrus (iOG)	0.01	0.9940
Basal Ganglia		
Basal Forebrain Nuclei (BF)*	9.71	3.87×10^{-18}
Putamen (Pu)*	7.00	5.10×10^{-11}
Cerebellum		
Cerebellum Crus I (CrusI)	0.75	0.4531
Cerebellum Crus II (CrusII)	0.74	0.4598
Cerebellum IV-Anterior Quadrangulate (CerIV)*	4.77	3.84×10^{-6}
Cerebellum III-Anterior Quadrangulate (CerIII)	2.26	0.0253
Rightward Asymmetry		
Frontal Cortex		
Posterior Superior Frontal Gyrus (pSFG)	-2.69	0.0077
Middle Inferior Frontal Gyrus (mIFG)	-0.20	0.8418
Lateral Orbitofrontal Cortex (lOFC)	-1.99	0.0486
Frontal Operculum (FOP)	-2.68	0.0081
Limbic Cortex		
Middle Cingulate Gyrus (MCC)	-0.37	0.7118
Posterior Cingulate Gyrus (PCC)*	-7.57	2.00×10^{-12}
Parahippocampal Gyrus (PHC)*	-5.24	4.50×10^{-7}
Amygdala (Amy)	-1.35	0.1803
Entorhinal Cortex (EG)*	-6.99	5.35×10^{-11}
Temporal Cortex		
Anterior Superior Temporal Gyrus (aSTG)	-1.47	0.1441
Posterior Superior Temporal Gyrus (pSTG)*	-6.32	2.04×10^{-9}
Anterior Middle Temporal Gyrus (aMTG)	-0.66	0.5117
Posterior Fusiform Gyrus (pFFG)**	-9.77	2.69×10^{-18}
Parietal Cortex		
Superior Postcentral Gyrus (sPoCG)	-3.00	0.0031
Middle Postcentral Gyrus (mPoCG)*	-3.71	0.0003
Superior Parietal Lobule (SPL)	-0.23	0.8186
Angular Gyrus (AG)	-1.04	0.2990
Parietal Operculum (POP)*	-6.03	9.51×10^{-9}

Paracentral Lobule (PCL)*	-12.67	1.32×10^{-26}
Precuneus (PCun)	-2.12	0.0355
Occipital Cortex		
Cuneus (Cun)*	-13.11	7.10×10^{-28}
Lingual Gyrus (LG)*	-8.98	4.02×10^{-16}
Calcarine Sulcus (Calc)*	-7.38	5.90×10^{-12}
Basal Ganglia		
Caudate Nucleus (CN)	-1.54	0.1264
Thalamus (Th)*	-9.10	1.81×10^{-16}
Globus Pallidus (GP)*	-8.57	4.89×10^{-15}
Nucleus Accumbens (NA)	-0.75	0.4553
Hypothalamus (HTh)	-0.04	0.9638
Cerebellum		
Cerebellum IX (CerIX)*	-5.57	9.18×10^{-8}
Cerebellum VIIIAB (CerVIIIAB)	-2.79	0.0059
Cerebellum VI (CerVI)*	-4.17	4.84×10^{-5}
Cerebellum V-Anterior B (CerVB)	-3.27	0.0013
Cerebellum V-Anterior A (CerVA)	-2.14	0.0341
Cerebellum II (CerII)*	-5.83	2.60×10^{-8}

Key: * multiple comparisons correction at FWE $p \leq 0.05$.

References

Ashburner J, Friston KJ. 2005. Unified segmentation. Neuroimage. 26:839–851.

Dahnke R, Gaser C. 2017. Voxel-based Preprocessing in CAT. Organ Hum Brain Mapp.

Dahnke R, Ziegler G, Gaser C. 2012. Local Adaptive Segmentation. Hum Brain Mapp Conf.

Gaser C, Dahnke R, Kurth K, Luders E, Alzheimer's Disease Neuroimaging Initiative. 2020. A computational Anatomy Toolbox for the Analysis of Structural MRI Data. Neuroimage. Under review

Manjon J V, Coupe P, Marti-Bonmati L, Collins DL, Robles M. 2010. Adaptive non-local means denoising of MR images with spatially varying noise levels. J Magn Reson Imaging. 31:192–203.

Rajapakse JC, Giedd JN, Rapoport JL. 1997. Statistical approach to segmentation of single-channel cerebral MR images. IEEE Trans Med Imaging. 16:176–186.

Rorder C, Brett M. 2000. Stereotaxic Display of Brain Lesions. Behav Neurol. 12.

Tohka J, Zijdenbos A, Evans A. 2004. Fast and robust parameter estimation for statistical partial volume models in brain MRI. Neuroimage. 23:84–97.